Energy dependence of the form factor for elastic electron scattering from ^{12}C

E.A.J.M. Offermann,[1,*] L.S. Cardman,[2] C.W. de Jager,[1]
H. Miska,[3,†] C. de Vries,[1] and H. de Vries,[1]
[1] *Nationaal Instituut voor Kernfysica en Hoge Energie Fysica (NIKHEF), Sectie K, P.O. Box 41882, 1009 DB Amsterdam, The Netherlands*
[2] *Nuclear Physics Laboratory and Department of Physics, University of Illinois at Urbana-Champaign, Champaign, Illinois 61820*
[3] *Institut für Kernphysik, Technische Hochschule Darmstadt, 6100 Darmstadt, Germany*
(Received 26 April 1991)

A static analysis of measurements of ^{12}C elastic electron-scattering cross sections demonstrates unambiguously the existence of a form-factor energy dependence beyond that due to Coulomb distortion effects. This energy dependence increases smoothly as a function of momentum transfer and incident energy in the region covered by the experiments ($1.0 < q_{\rm eff} < 2.3$ fm^{-1}, $240 < E_0 < 690$ MeV). Outside the first diffraction minimum the discrepancies between the form factors deduced from data obtained at different energies are as large as 5%; in the minimum discrepancies as large as 18% have been observed. Including dispersion corrections which are reasonably compatible with this observed energy dependence in the analysis of the data increases the rms charge radius deduced for ^{12}C by 0.007 to 2.478(9) fm, which is in excellent agreement with the value from muonic x-ray studies.

I. INTRODUCTION

High-energy electrons are an accurate probe of nuclear charge and current densities. This precision is due to the electromagnetic nature of the electron-nucleus interaction, which is calculable to high precision within the framework of quantum electrodynamics. Nuclear information is extracted from electron-scattering data in a one-hard-photon exchange treatment. This first Born approximation is improved by taking into account the distortion of the electron wave function by the Coulomb monopole field of the nucleus (the Coulomb correction, see Fig. 1) through a partial-wave analysis, which treats Coulomb effects to all orders. This approach, together with the correction of the measured spectra for radiative effects, will be referred to as a static analysis. Because the electromagnetic coupling constant is small ($\alpha \simeq \frac{1}{137}$), higher-order contributions to the electron-scattering process are traditionally neglected. To improve on the already impressive accuracy achieved in the analysis of elastic electron scattering data, the contribution of second-order (dispersive) effects must be investigated experimentally.

Dispersive effects arise from the fact that the nucleus is not rigid but has internal degrees of freedom that can be excited and deexcited virtually by the electron during the scattering process. They couple all possible nuclear excited states between the initial and final states of the nucleus, which renders a general calculation of their contribution to observed scattering cross sections a difficult task. All existing calculations of dispersion corrections have resorted to approximations to estimate the magnitude of these corrections. Typical approximations involve consideration of only a few strongly excited intermediate states, use of a simple nuclear model such as the harmonic-oscillator model, neglect of the excitation energy of intermediate nuclear states, and/or neglect of the contributions from the nuclear currents.

Several of these approximations were investigated by de Forest [1]. He calculated the dispersion correction for ^{16}O(e,e) up to second order in a harmonic-oscillator shell model for the nucleus, but keeping only the Coulomb part of the interaction. Two important results follow: (1) the contributions from the various nuclear levels to the dispersion corrections tend to cancel; and (2) accounting for the energy loss of the electron and the center-of-mass correction alters the results of the calculation significantly (both tend to reduce the magnitude of the dispersive corrections).

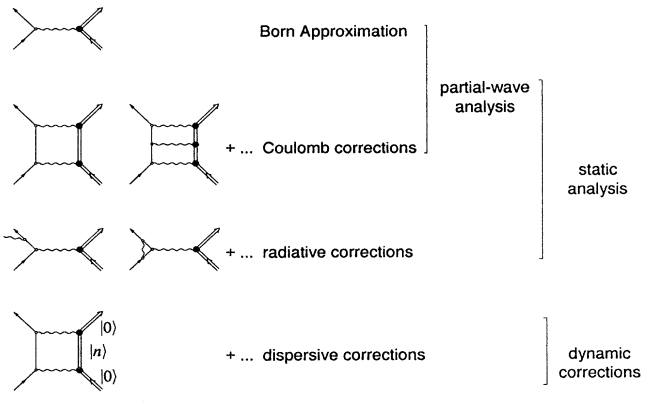

FIG. 1. Feynman diagrams for processes important in electron-nucleus scattering.

Although theoretical calculations often differ dramatically in their results, they agree on a number of general features of dispersion corrections. First, the form factor of the dispersive contribution is a smooth function of the momentum transfer between electron and nucleus, and is typically two orders of magnitude smaller than the first-order ("static") form factor. Therefore, dispersion corrections are largest (as a percentage of the cross section) in the region of diffraction minima where the first-order Born approximation has a zero and the electron-scattering cross section calculated in a static analysis is due entirely to higher-order Coulomb corrections. Second, the dispersive contribution tends to increase with increasing momentum transfer but to decrease with increasing incident electron energy. Finally, the importance of dispersion corrections in the region of diffraction minima decreases with increasing charge number Z because these corrections are calculated to be roughly proportional to α, while Coulomb corrections are proportional to αZ.

Dispersive contributions have been investigated in several earlier electron-scattering experiments. The cross-section ratios for elastic scattering from ^{207}Pb and ^{208}Pb were examined by Peterson *et al.* [2]. The cross sections measured for ^{207}Pb were up to 10% larger than those for ^{208}Pb; this was tentatively attributed to dispersive effects. Madsen *et al.* [3] measured cross-section values for elastic scattering from ^{142,146,150}Nd at low incident energies. Comparisons between their data and the predictions of a charge density obtained from a fit to data measured at higher energies showed that systematic discrepancies as large as 20% existed between the low- and high-energy data sets. Later experiments [4–7] indicated that most of the effects observed in these two measurements were due to errors in the cross section normalization, but some evidence remains for the presence of dispersive effects.

Another indication for dispersive effects in elastic electron scattering has also been reported by Sick and McCarthy [8], who investigated elastic scattering from ^{12}C and ^{16}O. They found it impossible to fit their data in the region of the first diffraction minimum with any charge distribution in a static analysis. The cross section in the minimum was observed to be about 12% higher than the predictions of their best-fit charge distribution. This effect has been confirmed qualitatively by a more recent study [9] of ^{12}C, which observed a discrepancy of 5% in the minimum.

A final indication for dispersive effects in electron scattering comes from the comparison of rms radii deduced from electron scattering and muonic atom studies [10,11]; the value inferred from the muonic atom experiment is nearly always larger than that from electron-scattering results. It has been suggested that this disagreement might be due to the neglect of dispersive contributions to the electron-scattering data and/or invalid approximations in the calculations of the corresponding effect (virtual nuclear excitation) in the muonic atom analysis.

None of the electron-scattering experiments to date has given conclusive evidence for the presence of dispersive effects. Second-order corrections to the one-photon exchange approximation have also been studied extensively theoretically, but the difficulty of performing such calculations without major approximations, together with the lack of sufficiently accurate data, leaves the results in doubt. The electron-scattering experiments reported here were designed specifically to study second-order effects in the hope that they would contribute to our understanding of higher-order processes. A further goal was to establish the size of dispersive contributions experimentally in order to set limits on errors in the extraction of nuclear densities from analyses of electron-scattering data in which higher-order processes in the reaction mechanism were neglected.

There is a general consensus that dispersive effects will be largest in the diffraction minima for elastic electron scattering from light nuclei. Calculations by Friar and Rosen [12] predict that the dispersive contributions have a very smooth energy and momentum-transfer dependence outside the diffraction minima. This characteristic explains part of the experimental difficulty in isolating these corrections; to the extent that they are purely dependent on momentum transfer, they can be largely absorbed in a static analysis of experimental data by a slight adjustment of the charge distribution parameters. These arguments motivate the present experiment, a highly accurate elastic electron-scattering experiment on ^{12}C in the region of the first diffraction minimum at different incident energies. ^{12}C is an obvious choice for such a study because elastic electron-scattering data have been obtained for ^{12}C over a large-momentum-transfer range; these data are essential for a systematic search for dispersive effects.

II. EXPERIMENT

In the present experiment, performed at the 500 MeV electron-scattering facility of NIKHEF-K [13], an effective momentum-transfer range 1.0–2.2 fm^{-1} was covered at two incident energies, around 240 and 430 MeV. Scattered electrons were analyzed with the high-resolution QDD spectrometer and its associated detection system. The properties of this system permit a determination of the complete electron kinematics after scattering. During every run the product of collected charge and target thickness was monitored continuously with the QDQ spectrometer, which shares a pivot with the QDD spectrometer. A disk of natural carbon with an isotopic purity of 98.9% and an average thickness of 93.3 mg/cm^2 was used as a target. The target was positioned in transmission geometry. Rotation of the target during the measurements and the use of a dispersed beam spot with a size between 5 and 15 mm resulted in an uncertainty in the average target thickness of less than 0.3%. The energy resolution $\delta E/E = 2 \times 10^{-4}$ allowed a clean separation of the ^{12}C elastic-scattering peak from contributions of ^{13}C.

The accurate determination of the kinematic variables is crucial for measurements in the region of a sharp diffraction minimum. Therefore, calibration measurements were performed before the runs as well as after every spectrometer rotation during the runs. In the sections that follow we discuss the calibration procedures

TABLE I. Contributions (in degrees) to the uncertainty in scattering angle.

	Optically determined	Sieve-slit determined
Spectrometer median plane	0.005	
Aperture location	0.01	
Central scattering angle Θ		0.02
θ_{tg} relative to Θ		< 0.02

and the uncertainties in these kinematic variables in detail.

A. Scattering angle calibration

Several factors contribute to the uncertainty in the scattering angle of the electron (see Fig. 2). The angle between the median plane of the spectrometer and the beam line was aligned optically and calibrated with respect to a fixed scale. This determined the angular position of the spectrometer median plane with an accuracy of 0.005°. The position of the spectrometer's solid-angle defining aperture relative to the median plane and the position of the center of rotation of the target system relative to the beam line were also determined optically. The errors in these quantities are listed in Table I.

The other parameters important for the event-by-event reconstruction of the scattering angle of the electrons were determined in measurements with a special, solid-angle defining "sieve slit" [14]. The main purpose of the sieve-slit measurements was the determination of the optical transfer matrices for the QDD spectrometer that are used to reconstruct the electron vector. These measurements also proved to be important in the determination of the central scattering angle Θ because they provided a very sensitive test for a possible misalignment of the center of rotation of the target system and the center of rotation of the spectrometer [14]. As a result of sieve-slit calibrations after each spectrometer rotation, the central scattering angle Θ was reproducible to $\pm 0.02°$ and the angle θ_{tg} (between the electron vector and the central scattering angle as measured in the scattering plane) could be reconstructed with an accuracy of $\pm 1\%$. This resulted in an uncertainty in θ_{tg} less than $\pm 0.02°$ even for the largest solid-angle defining aperture used.

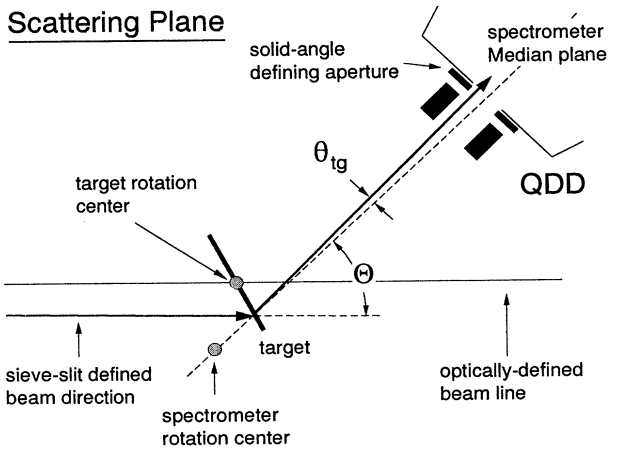

FIG. 2. Schematic layout of the scattering plane showing the angles that are relevant to the definition of the scattering angle.

B. Energy calibration

The incident energy of the electrons and the spectrometer constants were determined in a single, consistent framework using measurements that were performed during the actual data taking, thereby minimizing systematic errors. Calibration data were taken with beryllium-oxide, boron-nitride, and tantalum targets at each scattering angle. The recoil energy differences measured for these isotopes and excitation energies taken from the literature provided the information necessary for an accurate determination of the energy of the incoming electron beam and of the electrons detected along the spectrometer's focal plane.

The position, x (channel number), along the focal plane is related to E_f, the energy of the detected electron, through the dispersion polynomial:

$$E_f = \Gamma B \left(1 + \sum_{j=1}^{4} d_j (x - x_c)^j \right) . \quad (1)$$

Here, Γ is the conversion factor (in MeV/kG) between the spectrometer's magnetic field B (in kG) and the energy of the particles following the central trajectory; the d_j ($j = 1 - 4$) are the spectrometer dispersion coefficients (in chan^{-j}); and x_c is the number of the central-channel ($x_c = 2200$).

For each peak, the energy E_f (in MeV) is expressed in terms of its corresponding excitation energy E_x and the incident beam energy E_0:

$$E_f = \frac{1}{\eta} \left[E_0 - \frac{E_{\rm loss}}{2} - E_x \left(1 + \frac{E_x}{2M} \right) \right] - \frac{E_{\rm loss}}{2} \quad (2)$$

with M the mass of the target nucleus (in MeV). The factor η is the recoil factor:

$$\eta = 1 + \frac{(2E_0 - E_{\rm loss}) \sin^2(\theta/2)}{M} ;$$

$E_{\rm loss}$ is the mean energy loss (in MeV) due to Landau straggling in the target in transmission geometry:

$$E_{\rm loss} = c_1 \frac{Z}{A} t \left[\ln \left(c_2 \frac{t}{\rho} \right) \right] ,$$

where the constants c_1 and c_2 have values of 0.154 MeV cm^2/g and 2.31×10^8 cm^{-1}, respectively; t is the effective target thickness (in g/cm^2); and ρ is the target density (in g/cm^3).

The parameters E_0, Γ, and d_j (j=1–4) are determined simultaneously using Eqs. (1) and (2) in a least-squares fit of the energy-calibration data. There is a strong corre-

lation between the beam energy E_0 and the spectrometer constant Γ, so it is necessary that the data cover a wide range of values of the recoil factor in order to obtain a precise estimate of the energy E_0. Table II lists the values of E_0 and Γ obtained for the different experimental runs. The errors listed are statistical only, and include the effects of the correlations between the variables.

There seems to be a systematic deviation between the values of Γ obtained at different magnetic-field settings; it is systematically larger for the runs at 430 MeV (I, III, and V) than for the runs at 240 MeV (II and IV). This apparent field dependence of the conversion factor Γ is probably due to a difference in the magnetic-field configuration caused by the cycling procedure and/or saturation effects. The systematic uncertainty in E_0 can be estimated by comparing the fitted value of the spectrometer constant Γ between different experimental runs at the same magnetic-field setting. The values of Γ in Table II indicate that this error in E_0 is less than 0.08%.

TABLE II. Energy-calibration parameters and their statistical uncertainties for different experimental runs.

Run	Γ (MeV/kG)	E_0 (MeV)
I	42.031(6)	418.80(7)
II	41.960(8)	238.13(5)
III	42.034(7)	431.44(7)
IV	41.994(16)	242.73(9)
V	42.010(13)	428.83(18)

III. DATA ANALYSIS

In the analysis of previous measurements [8, 9] one of the factors that hampered the unambiguous identification of an energy dependence of the form factor in the minimum was the correction for the finite solid angle of the spectrometer. The cross-section differences observed ranged from 5 to 12% but folding corrections as large as 12% were applied in the data analysis. The data-taking and analysis procedure used in the present experiment limited the folding corrections to 2%, even at the highest incident energies.

Another important ingredient in our data set is the fact that the normalization between runs at different energies is well known. Previous experiments above q=1 fm^{-1} consist of separate data sets measured at different incident energies with only a limited overlap of the momentum-transfer range. The relative normalization of these data sets is not known exactly. As a consequence, a large part of the dispersive effects in these data could have been concealed by a renormalization of the form-factor data sets in a combined analysis. The procedure by which the normalizations between the data sets and contributions to their uncertainties were established is discussed in detail below.

A. Histogramming of the solid angle

During the experiment, information from the detection-system was stored event by event for off-line analysis. The detection system of the QDD spectrometer permits reconstruction of the momentum, direction, and position (in the nondispersive direction only) at the target for each detected electron [13, 15]. The coordinate of the scattering point in the plane of the spectrometer's dispersion cannot be reconstructed because the spectrometer is operated "dispersion matched" to the incident electron beam. Therefore, the out-of-plane angle ϕ_{tg} was folded with a $\pm$7.5-mrad-wide distribution corresponding to the angular uncertainty associated with the maximum beam-spot size of 15 mm.

The event-by-event trajectory information can be used to subdivide the solid-angle acceptance of the spectrometer into bins, each covering a small range of scattering angles [see Fig. 3(a)]. Using this procedure, a single set-

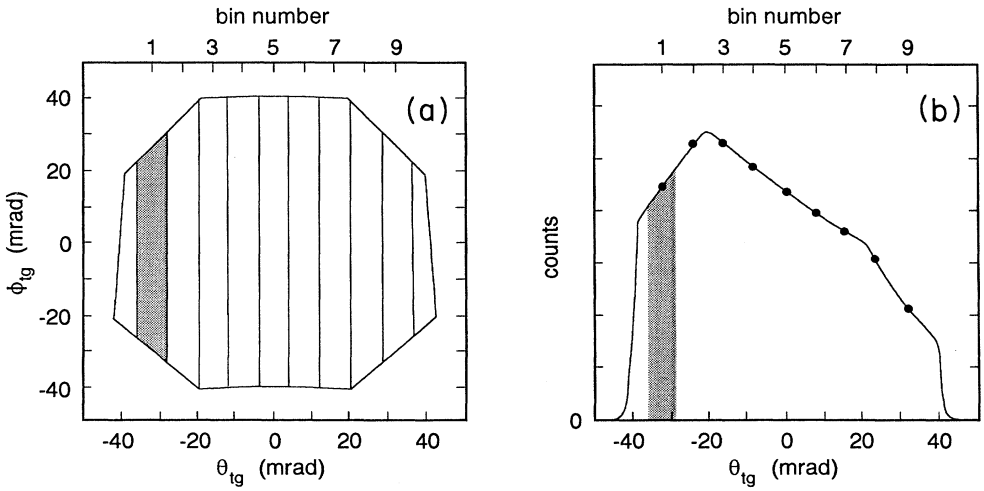

FIG. 3. (a) The acceptance of the largest aperture used in the scattering plane (θ_{tg}) and the dispersive plane (ϕ_{tg}). The $\Delta\theta_{tg}$ bins into which the solid angle was divided in the data analysis are indicated. (b) The number of electrons scattered from ^{12}C observed with the QDD using the solid-angle defining aperture of (a) is shown as a function of the measured angle θ_{tg}. The gray bands in the two figures indicate one of the $\Delta\theta_{tg}$ bins into which the data were histogrammed.

ting of the spectrometer provides a number of data points [see Fig. 3(b)]. This histogramming procedure is an indispensable tool for measuring cross sections in the region of a diffraction minimum because the scattering-angle range of each bin can be chosen small enough that the folding correction for the cross section measured for that bin is small and accurately calculable.

The width of the scattering-angle bin was chosen on the basis of the angular resolution of the QDD, the multiple-scattering contribution from the target, and the folding correction. The QDD has a ±2-mrad resolution in the scattering plane [14]. For an effective target thickness of about 130 mg/cm^2 the rms value of the multiple-scattering angle is less than 5 mrad for the energies and scattering angles of the present experiment. Therefore, we have chosen to histogram the data into 8-mrad bins. In all cases, even in the minimum, these bins were small enough that the folding correction remained $\leq 2\%$ despite the strong scattering-angle dependence of the cross section. To minimize edge effects on the solid angle of the bins, the outer bin edges in the scattering plane were always positioned at least 4 mrad from the edges of the solid-angle defining aperture. In the five data runs three different sizes of solid-angle defining apertures were used, as listed in Table III. The choice of scattering-angle bins results in nine cross-section data points at each spectrometer setting for apertures B and C [see Fig. 3(a)]. At the five most-forward scattering-angle positions of the spectrometer at 430 MeV, a smaller aperture (A) with a scattering-angle acceptance of 20 mrad had to be used to limit the count rate. Dead-time corrections never exceeded 10% and could be calculated very accurately due to installation of a large, fixed dead-time of 500 ns in the trigger logic of the detection system. When the small aperture A was used, only one data point was derived from a single bin of 12 mrad. For all of the measurements, except for the above-mentioned five spectrometer settings at the most-forward angles, overlapping data points were obtained by rotating the spectrometer's central angle through an angle smaller than the scattering-angle acceptance of the solid-angle defining aperture; this provided an important stability check for the experimental setup.

TABLE III. Nominal acceptances of the solid-angle defining apertures.

Aperture	$\Delta\theta_{tg}$ (mrad)	$\Delta\phi_{tg}$ (mrad)
A	20.0	20.0
B	80.0	16.0
C[a]	80.0	80.0

[a]This aperture has an octagonal shape.

B. Calculation of the cross sections

A momentum spectrum is obtained for each scattering-angle bin. The cross sections for the ground state and excited states of a particular nucleus were determined by fitting each spectrum with a sum of hyper-Gaussian and Lorentzian peak shapes convoluted with their radiative tails, as shown in Fig. 4. The radiative tail used was a convolution of the effects of Landau straggling [17], exter-

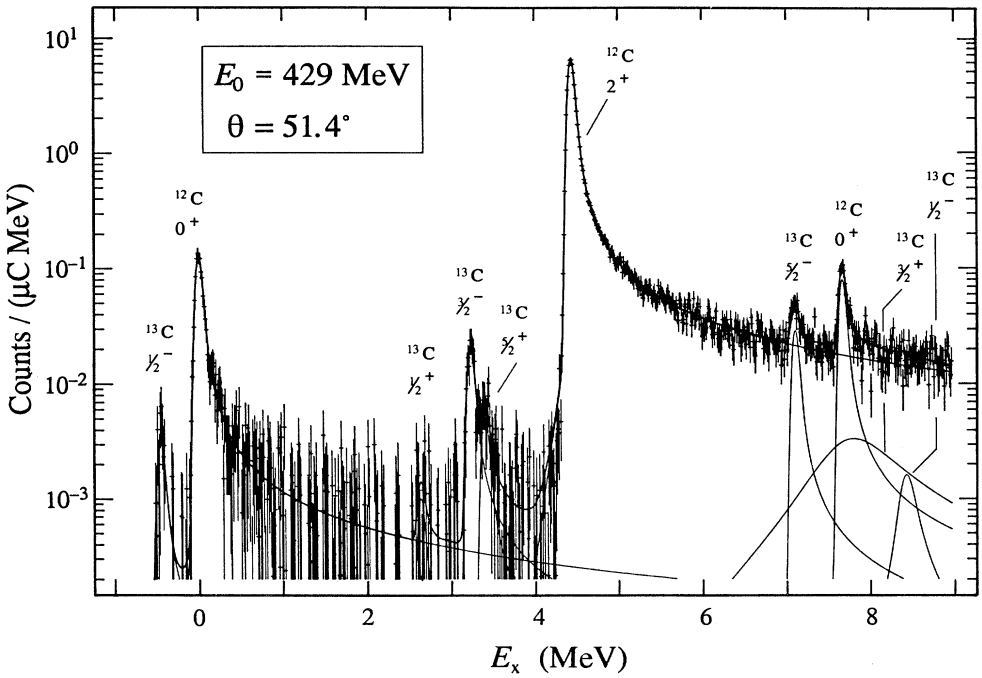

FIG. 4. The spectrum of electrons scattered from the graphite target into bin 1 [see Fig. 3(a)] as a function of the excitation energy in ^{12}C. Also shown are the individual line shapes fitted to the spectrum. Scattering from the $\sim 1\%$ ^{13}C contaminant is separated cleanly from the ^{12}C scattering.

nal bremsstrahlung [18], and the Schwinger [19] corrections. The peak shapes provided a good fit to all known levels [16] of ^{12}C and ^{13}C in the excitation region studied.

The cross sections must be corrected for the efficiency of the focal-plane detection system. Insufficient or improper response of the focal-plane detectors can result in the rejection of events due to incomplete focal-plane information or incorrect reconstruction of focal-plane coordinates. The first effect influences the absolute efficiency of the QDD detection system, which was determined [13] to be $97.1 \pm 0.4\%$. The second effect results in events being placed in the wrong momentum bin and/or in their being traced back to the wrong scattering-angle bin. This effect was smoothed out to a large extent by shifting the detector package periodically during the measurements. Remaining fluctuations were further reduced by monitoring the drift-time pattern in each wire chamber for each event. Events with an anomalous pattern were rejected. The fraction of events rejected by this check was typically 0.5%, and was constant over the scattering-angle bins.

The precise reconstruction of the scattered electron's vector at the target allowed well-defined cuts on the angles by which an electron enters the solid angle of the spectrometer. Figure 5 shows a three-dimensional histogram of the reconstructed electron angles at the target for a measurement with the octagonal aperture C. Note that the central peak in this figure is truncated at 2% of its height to enhance the visibility of possible background events outside the acceptance of the aperture. Since most background events are produced at or near the target and have lost energy before detection by rescattering in the spectrometer or the entrance collimator, or by hitting material positioned close to the target, they are distinguished by their coordinates in the dispersive plane of the spectrometer.

A peak around $\phi_{tg} = -90$ mrad and a continuum above $\phi_{tg}=+55$ mrad are evident in Fig. 5 in addition to the dominant central peak associated with "good" electron events. The momentum spectra associated with the three indicated ranges of values for the dispersive angle ϕ_{tg} are shown in the right half of the figure. The peak at -90 mrad is caused by a halo of the incoming electron beam hitting the thick aluminium rings that support the graphite target. These events were always $< 0.3\%$ of the total observed. The continuum above +55 mrad comes from combining data from different events in the different wire chambers in the reconstruction of the particle vector at the focal plane. Its size depends on the count rate [20], but never exceeded 0.5% of the elastic cross section. These events were rejected in the off-line analysis by applying a ± 55 mrad window on ϕ_{tg}.

The solid-angle defining aperture of the QDD spectrometer is located between the entrance quadrupole and the first dipole magnet. As a consequence, the solid-angle acceptance depends on the momentum of the detected electrons. The effect of the quadrupole was calculated by ray-tracing particles from the target through the quadrupole to the aperture using the program RAYTRACE [21] and the design value for the quadrupole's magnetic field configuration. The solid angle for each scattering-angle bin varied less than $\pm 1\%$ over the momentum acceptance of the spectrometer. The corrections were checked by evaluating the cross sections for the first excited state in ^{12}C, as discussed in Sec. III E.

The product of collected charge and target thickness was monitored continuously during the experiment with the QDQ spectrometer. For the runs I and III the QDQ spectrometer was tuned to detect electrons, while for the runs IV and V it was used to detect knocked-out protons instead; this was found to provide a better long-term

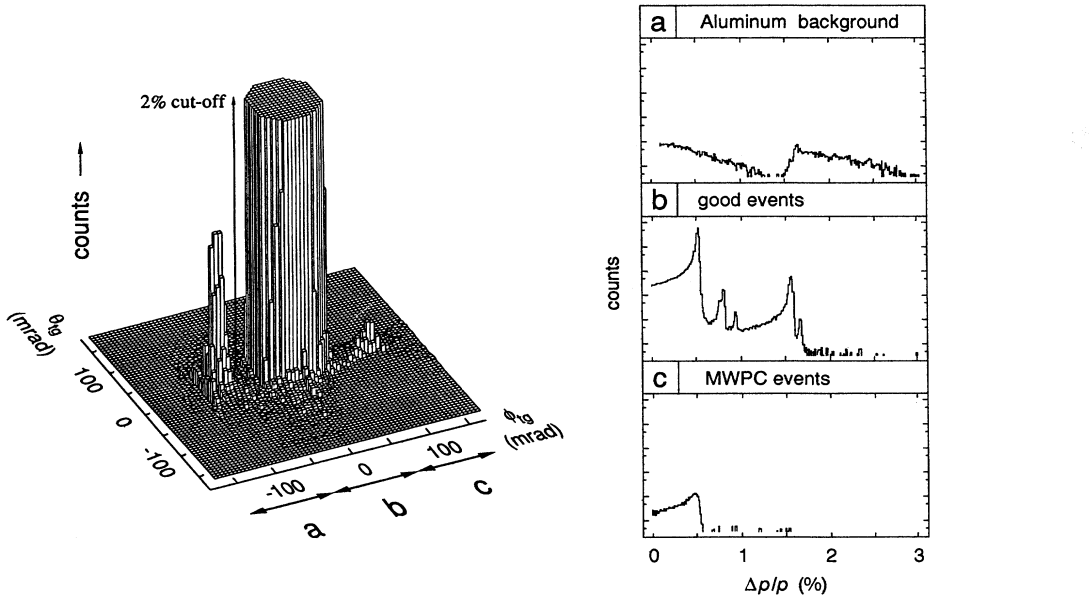

FIG. 5. A three-dimensional histogram of the reconstructed angle coordinates at the target for a measurement with an octogonal aperture. The central peak is cut off at 2% of its height. The three inset figures show the momentum spectra of the electrons associated with the cuts a, b, and c indicated on the ϕ_{tg} coordinate.

stability. A correction factor for the variations in the product of collected charge and target thickness was calculated from the ratio of the number of event triggers in the QDQ per unit of collected charge to its mean value during the run.

The correction factors for runs I, III, IV, and V are shown in Fig. 6 as a function of the effective momentum transfer q_{eff}, where

$$q_{\text{eff}} = \frac{2E_0 \sin(\theta/2)}{\eta^{1/2}} \left(1 + \frac{3}{2} \frac{Ze^2}{\left(\frac{5}{3}\right)^{1/2} \langle r^2 \rangle^{1/2} E_0}\right) \quad (3)$$

with $\langle r^2 \rangle^{1/2}$ the rms charge radius. The fluctuations in the correction factor are roughly consistent with the 0.3% inhomogeneity of the graphite target. For run II and the two lowest q_{eff} values in run IV no correction factor is available due to malfunctions of the QDQ detection system. However, a stability check of the experimental setup that includes these measurements is discussed in the next section.

C. Stability of the experimental setup

The corrections discussed above should have removed any dependence of the cross sections on the position in the focal plane where the corresponding peaks were detected and on the scattering-angle bin for which the momentum spectrum was determined. This has been checked by studying the cross sections for the 2^+ excitation in ^{12}C at E_x=4.439 MeV, which were measured simultaneously with the elastic-scattering data.

For this study the count-rate response of scattering-angle bin (i) at spectrometer angle setting (j), $\varepsilon^{ij}_{\Delta\theta}$, has been defined to be the product of a correction factor c_j, which includes all factors related to the instability of the experimental setup at spectrometer angle setting (j) and $\varepsilon^{i}_{\Delta\theta}$, the response of scattering-angle bin (i), which includes irregularities due to the histogramming procedure. The response function $\varepsilon^{i}_{\Delta\theta}$ has been determined separately for each of the different solid-angle defining apertures for each of the five experimental runs.

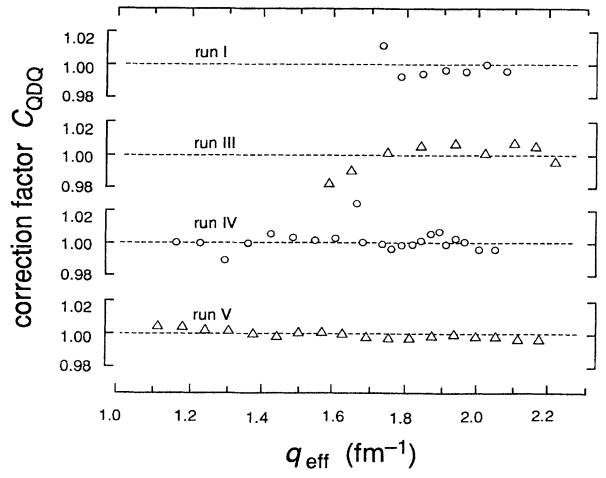

FIG. 6. Correction factor C_{QDQ} for the run-to-run fluctuations in the product of the collected charge and the target thickness as a function of q_{eff}.

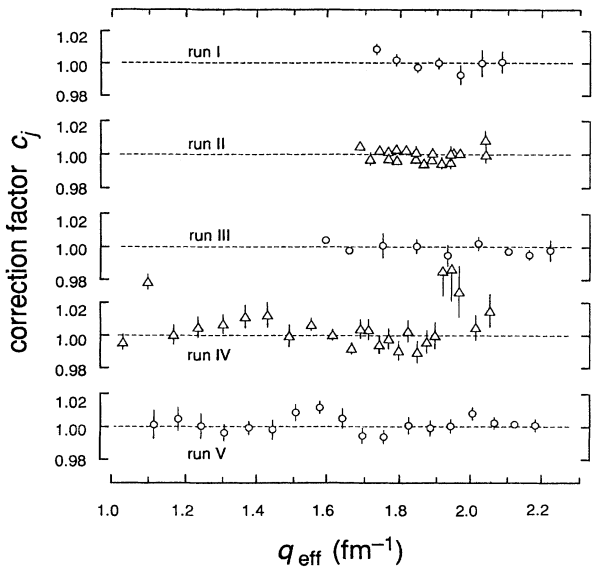

FIG. 7. Correction factors c_j for the instability of the QDD detection system at different spectrometer angle settings as a function of q_{eff}.

The count-rate response $\varepsilon^{ij}_{\Delta\theta}$ was determined by parametrizing the 2^+ cross sections with a Fourier-Bessel fit for each experimental run, using the computer code HADES [22]. In this fit only the five scattering-angle bins of each spectrometer setting that were positioned in the center of the solid-angle acceptance were used, minimizing the influence of possible small errors in the histogramming procedure. The count-rate response $\varepsilon^{ij}_{\Delta\theta}$ was calculated from the ratio of the experimental 2^+ cross section and the calculated value. The coefficients c_j and $\varepsilon^{i}_{\Delta\theta}$ were determined in a χ^2 fit of the count-rate response.

The correction factor c_j is shown in Fig. 7 for the different experimental runs. The small fluctuations in this correction factor confirm the stability of the experimental setup. The larger deviation at the second spectrometer setting in run IV might be due to the fact that here no QDQ correction factor was available (see Sec. III B). Fluctuations as large as ±0.5% can result from the influence of the beam-spot size in the dispersive direction on the solid angle; no explicit corrections were made for this effect in the analysis.

The bin-response function $\varepsilon^{i}_{\Delta\theta}$ is represented in Fig. 8 by the open circles for aperture C for the runs I and II. Clearly $\varepsilon^{i}_{\Delta\theta}$ depends on θ_{tg} with the outer bins showing significant correction factors. The θ_{tg} dependence for aperture B agrees qualitatively with the result for aperture C, but deviations from unity are much smaller. This dependence is probably due to small deviations of the actual quadrupole-magnet field from its design value which was used to calculate the solid angle.

Possible field deviations were investigated in first order by varying the linear part of the transformation

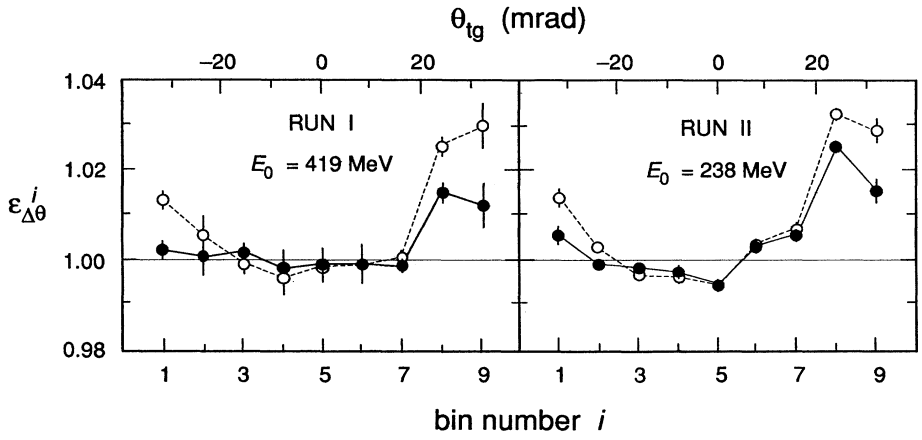

FIG. 8. The response $\varepsilon^i_{\Delta\theta}$ of the scattering bin before [open circles (o)] and after [closed circles (•)] correction for the θ_{tg} reconstruction.

of the scattering angle θ_{tg} from the position after the quadrupole to the target [14]. In a χ^2 fit the influence of θ_{tg} on both the solid angle and the count-rate response is taken into account. Fits were performed only for measurements with aperture C because here the deviation of the scattering angle θ_{tg} is determined most precisely since it influences both the count-rate response (through a change in the fitted cross section) and the solid angle of a bin (due to the tapered edges of aperture C).

The correction to the angle θ_{tg} is listed for each run in Table IV. This correction is in agreement with calibration measurements for the quadrupole field reported by Offermann *et al.* [14]. The bin responses $\varepsilon^i_{\Delta\theta}$ after correction for the change in θ_{tg} are indicated by the solid circles in Fig. 8. The remaining (asymmetric) deviation from unity can be attributed to an incorrect angle reconstruction. However, the corresponding error in the reconstruction of the angle θ_{tg} is still within the estimated 1% uncertainty (see Table I).

In summary, the study of the count-rate response resulted in a correction to the cross sections for each spectrometer setting (see Fig. 7), a correction to the scattering angle θ_{tg} (see Table IV), and a cross section correction for the remaining variations of the bin-response function (see solid circles in Fig. 8).

The energy dependence of the normalization of the data accumulated in the different experimental runs was investigated by a distorted-wave Born approximation analysis of the 2^+ data at 240 and 430 MeV (accumulated simultaneously with the elastic scattering data). In this analysis the (transverse) $E2$ contribution to the dominantly $C2$ excitation was taken into account through a parametrization of the electric current obtained from the 180° scattering data of Flanz *et al.* [23]. This correction was always less than 0.5% for the angles and energies of the present experiment. The 2^+ data were corrected with the results from the count-rate response measurements described above. Different normalization coefficients were introduced for measurements with different solid-angle defining apertures. The normalizations were determined relative to the data of run II. The results are listed in Table V. The high-energy data measured with apertures A and B are consistent with the low-energy data measured with aperture C. The high-energy data measured with aperture C all show a 2% lower normalization factor than the rest of the data. The large dimensions of this aperture in the dispersive angle ϕ_{tg} suggest that an energy dependence of the higher-order transfer coefficients may be responsible for this difference.

The combined results of Tables IV and V indicate a difference of 2.6% in the acceptance of the software-defined angle bins at the two energies. In a previous experiment, also at 430 MeV, a sieve-slit study [14] yielded a 2.0(1.4)% smaller acceptance than the design value.

TABLE IV. Rescaling of the angle θ_{tg} relative to the central scattering angle.

Run	E_0 (MeV)	$\Delta\theta_{tg}$ (%)
I	418.80	−1.3(1)
II	238.13	−0.9(1)
III	431.44	−1.7(1)
IV	242.73	−0.9(2)
V	428.83	−1.6(1)

TABLE V. Overall normalization factors for the different data sets. The normalization factor for a data set is defined as norm = $\sigma_{\rm fit}/\sigma_{\rm exp}$.

		Normalization		
	E_0	Full aperture: $[\Delta\theta_{tg},\Delta\phi_{tg}$ (mrad)]		
Run	(MeV)	A: (20,20)	B: (80,16)	C: (80,80)
I	418.80			1.020(2)
II	238.13			1.000
III	431.44			1.026(2)
IV	242.73			1.002(2)
V	428.83	0.998(5)	1.005(2)	1.016(2)

These observations lead us to decide to normalize all data to the 240-MeV data using the correction factors given in Table V.

D. Unfolding of energy and angle spread

Each measured cross section differs from its "true" value due to the fact that the experiment integrates the cross section over the scattering angles subtended by the finite aperture of the spectrometer and the angular divergence of the incident beam (including multiple scattering in the target itself) and also integrates over the energy resolution of the beam and the experimental apparatus. The data were corrected for these effects using the method of Lyman, Hanson, and Scott [24] in an iterative procedure in which the slope and curvature of the cross section with respect to scattering energy and scattering angle was determined self-consistently from this experiment. In this method the cross-section behavior is first determined with the uncorrected data points. The slope and curvature of the cross sections with respect to energy and angle are calculated using the ground-state charge density that provided a best fit to these data. These cross-section derivatives are then used to perform an unfolding correction to first order:

$$\sigma_{\rm fol} = \sigma_{\rm unfol}\left\{1+\frac{\sigma_{1\theta}}{4}\cot\Theta\left[\varepsilon^2+\frac{(\Delta\phi_{tg})^2}{6}\right]+\frac{\sigma_{2\theta}}{4}\left[\varepsilon^2+\frac{(\Delta\theta_{tg})^2}{6}\right]+\sigma_{2E}\frac{(\Delta E)^2}{24}\right\}, \tag{4}$$

where

$\sigma_{\rm fol}$ = the cross section integrated over scattering energy and angle,
$\sigma_{\rm unfol}$ = the unfolded cross section,
Θ = the central scattering angle of the bin,
$\Delta\phi_{tg}$ = the angular width of the bin in the dispersive plane,
$\Delta\theta_{tg}$ = the angular width of the bin in the scattering plane,
ε = the rms value of the multiple-scattering angle [24],
ΔE = the energy spread of the incoming beam,
$\sigma_{1\theta}=\frac{1}{\sigma}\frac{\partial\sigma}{\partial\theta}$, $\sigma_{2\theta}=\frac{1}{\sigma}\frac{\partial^2\sigma}{\partial\theta^2}$, and $\sigma_{2E}=\frac{1}{\sigma}\frac{\partial^2\sigma}{\partial E^2}$.

This correction never exceeded 2% due to the small size of the solid-angle acceptance. As a result, the procedure converged in a single iteration.

After all corrections were performed, data points from overlapping spectrometer settings were combined. Cross sections obtained at slightly different angles, and energies were converted to the same angle and energy setting by using a logarithmic expansion up to second order of the cross section [25]. The experimental cross sections are listed in Table VI.

E. Cross section uncertainties

Statistical and systematic uncertainties in the cross-section data are discussed in this section. A distinction is made between errors resulting from normalizations relevant for intercomparison of the cross sections measured in the present experiment and from an overall normalization necessary for the interpretation of the data in terms of absolute cross sections. In the following analysis the error contributions from the relative normalizations were used because the absolute normalization is determined by the inclusion of existing, high-precision, low-q data sets in the analysis.

Table VII summarizes the sources of uncertainty in the relative normalization. As discussed in Sec. II, the uncertainty in the scattering angle has several contributions. The contributions from the uncertainty in the median plane are systematic, but the contributions from the other two uncertainties in the scattering angle can be treated as statistical since the final cross section is the average of several cross-section values obtained from overlapping scattering-angle bins. These scattering-angle bins were positioned differently with respect to the median plane, so that the errors in the reconstructed angle contribute in different directions to the cross section. The same argument holds for the uncertainty in the scattering angle due to the position of the beam spot and for the normalization factors determined with the data of the 2^+ level and the data from the QDQ spectrometer.

The statistical uncertainty in the incident energy was obtained from a least-squares fit to the energy-calibration data; the systematic error in the energy was estimated from the variation of the spectrometer constant Γ at the same incident energy, as discussed in Sec. II. The uncertainty in the cross section was determined from the energy and angle uncertainties through the cross-section dependence on these parameters. The overall statistical uncertainties in the cross sections were taken to be the quadratic sum of the effects of the statistical uncertainties listed in Table VII and the counting statistics. The overall systematic error in the data was taken to be the linear sum of the systematic errors listed in Table VII.

The uncertainties in the absolute normalization of the data are summarized in Table VIII. A distinction is made between normalization uncertainties which change all cross sections in the same direction (σ_1) and uncertainties which can change the normalization of individ-

ual data points in either direction (σ_{II}). We have estimated that the theoretical uncertainty in the radiative correction contributes 0.1% to σ_I. The contribution of the radiative correction to σ_{II} is of a completely different nature. If scattering of the electron is preceded by energy loss through radiation, the scattering takes place at an effectively lower energy. Our radiative corrections do not take into account the associated change in the value of the form factor for this process. Calculations by Merle [25] and Reuter [26] suggest that these processes result in corrections smaller than $\pm 0.3\%$ for our kinematic conditions. This was taken into account by adding 0.3% to σ_{II}.

IV. ENERGY DEPENDENCE OF THE ^{12}C ELASTIC FORM FACTOR

A. Ground-state charge density parametrization

The validity of the static analysis can be investigated by comparing the ^{12}C elastic cross sections measured at two energies over the same momentum-transfer range. A charge density is derived from the data set at the first energy and then used to predict the cross-section values for the same momentum transfers at the second energy. Cross sections are calculated by partial-wave solution of the Dirac equation which contains the Coulomb potential

TABLE VI. Cross sections for elastic electron scattering from ^{12}C. The corrections discussed in Sec. III have been applied.

θ (deg)	$d\sigma/d\Omega$ (fm^2/sr)	Uncertainty Statistical (%)	Uncertainty Systematic (%)	θ (deg)	$d\sigma/d\Omega$ (fm^2/sr)	Uncertainty Statistical (%)	Uncertainty Systematic (%)
	E_0 = 238 MeV				E_0 = 243 MeV		
84.94	8.379×10^{-7}	1.3	0.9	46.54	1.435×10^{-3}	0.8	1.8
85.63	6.973×10^{-7}	0.9	0.9	47.23	1.278×10^{-3}	0.6	1.8
86.53	5.439×10^{-7}	0.9	0.9	48.14	1.092×10^{-3}	0.6	1.8
87.43	4.142×10^{-7}	0.8	1.0	49.06	9.178×10^{-4}	0.6	1.8
88.33	3.173×10^{-7}	0.8	1.1	49.96	7.845×10^{-4}	0.5	1.7
89.23	2.347×10^{-7}	1.0	1.1	50.83	6.748×10^{-4}	0.6	1.5
90.13	1.730×10^{-7}	0.9	1.2	51.74	5.771×10^{-4}	0.6	1.5
91.03	1.247×10^{-7}	0.8	1.3	52.66	4.917×10^{-4}	0.6	1.5
91.93	9.003×10^{-8}	0.8	1.4	53.56	4.136×10^{-4}	0.5	1.5
92.83	6.164×10^{-8}	0.8	1.4	54.43	3.511×10^{-4}	0.6	1.5
93.74	4.272×10^{-8}	0.9	1.5	55.34	2.998×10^{-4}	0.6	1.5
94.66	2.854×10^{-8}	1.0	1.5	56.26	2.540×10^{-4}	0.7	1.5
95.55	2.009×10^{-8}	1.0	1.4	57.16	2.136×10^{-4}	0.5	1.5
96.42	1.480×10^{-8}	1.0	1.1	58.03	1.820×10^{-4}	0.7	1.2
97.34	1.216×10^{-8}	1.0	0.6	58.94	1.551×10^{-4}	0.7	1.3
98.26	1.138×10^{-8}	1.0	0.3	59.86	1.315×10^{-4}	0.7	1.3
99.14	1.252×10^{-8}	1.0	0.7	60.76	1.104×10^{-4}	0.6	1.2
100.03	1.453×10^{-8}	1.1	0.9	61.62	9.320×10^{-5}	0.7	1.0
100.94	1.695×10^{-8}	1.0	1.0	62.54	7.964×10^{-5}	0.8	1.0
101.86	2.000×10^{-8}	1.1	0.9	63.46	6.661×10^{-5}	0.8	1.0
102.75	2.371×10^{-8}	1.0	0.9	64.36	5.459×10^{-5}	0.8	1.0
103.63	2.641×10^{-8}	1.1	0.8	65.23	4.733×10^{-5}	0.9	0.9
104.54	3.029×10^{-8}	1.1	0.7	66.14	3.973×10^{-5}	0.9	0.9
105.46	3.285×10^{-8}	1.3	0.7	67.06	3.334×10^{-5}	1.0	0.9
106.38	3.471×10^{-8}	1.4	0.6	67.96	2.728×10^{-5}	0.8	0.9
111.37	4.576×10^{-8}	1.2	0.4	68.83	2.274×10^{-5}	1.0	0.9
112.28	4.510×10^{-8}	1.1	0.3	69.74	1.919×10^{-5}	1.0	0.9
113.20	4.493×10^{-8}	1.1	0.3	70.66	1.582×10^{-5}	1.1	0.9
114.11	4.532×10^{-8}	1.1	0.3	71.56	1.323×10^{-5}	0.9	0.9
114.80	4.591×10^{-8}	1.8	0.3	72.43	1.097×10^{-5}	1.0	0.9
				73.34	9.122×10^{-6}	1.0	0.9
				74.26	7.452×10^{-6}	1.1	0.9
				75.19	5.998×10^{-6}	1.0	1.0
				76.13	4.797×10^{-6}	1.0	1.0
				77.04	3.972×10^{-6}	1.1	1.0
				77.96	3.222×10^{-6}	1.1	1.0
				78.84	2.577×10^{-6}	1.0	1.2
				79.63	2.110×10^{-6}	1.1	1.6

of a static nucleus with a spherically symmetric charge distribution but without internal degrees of freedom.

The best-fit charge density was obtained by performing a χ^2 analysis of the data using the phase-shift program MEFIT [25]. In this phase-shift analysis the charge distribution parameter variations were explicitly constrained to keep the gradient of the charge distribution zero at the cutoff radius beyond which this distribution is zero. In those data sets where the incident energy was varied, the nominal value of the energy together with its quoted uncertainty was included as an additional data point in the χ^2 fit. The electron mass was neglected in the phase-shift calculations for computational simplicity. However, an empirical correction factor [27] for the finite electron mass, which is valid to an accuracy of better than 0.04% for the kinematical conditions of this experiment, was applied to the calculated cross sections; this correction factor never exceeded 0.2%.

The numerical accuracy of the phase-shift calculations has been checked by comparing the results of the program MEFIT with those of the phase-shift code HADES [22]. The results of the two programs are in perfect agreement.

TABLE VI. *(Continued).*

θ (deg)	$d\sigma/d\Omega$ (fm^2/sr)	Uncertainty Statistical (%)	Uncertainty Systematic (%)	θ (deg)	$d\sigma/d\Omega$ (fm^2/sr)	Uncertainty Statistical (%)	Uncertainty Systematic (%)
	E_0 = 419 MeV				E_0 = 429 MeV		
45.52	3.630×10^{-6}	1.4	2.3	29.43	1.630×10^{-3}	0.9	1.2
45.98	2.802×10^{-6}	1.5	2.4	31.23	8.976×10^{-4}	1.0	1.2
46.44	2.111×10^{-6}	1.6	2.4	33.03	4.877×10^{-4}	1.0	1.2
46.90	1.554×10^{-6}	1.7	2.5	34.83	2.572×10^{-4}	1.0	1.2
47.34	1.177×10^{-6}	1.2	2.5	36.72	1.280×10^{-4}	0.7	1.3
47.80	8.589×10^{-7}	1.3	2.6	37.68	8.761×10^{-5}	1.0	1.1
48.25	6.090×10^{-7}	1.4	2.6	38.35	6.724×10^{-5}	1.0	1.2
48.71	4.234×10^{-7}	2.0	2.7	38.82	5.568×10^{-5}	1.1	1.2
49.16	2.889×10^{-7}	1.5	2.5	39.27	4.592×10^{-5}	1.1	1.2
49.60	2.050×10^{-7}	1.6	2.6	39.73	3.784×10^{-5}	1.1	1.2
50.06	1.384×10^{-7}	1.6	2.5	40.17	3.089×10^{-5}	0.9	1.2
50.51	1.045×10^{-7}	1.6	2.2	40.62	2.561×10^{-5}	1.0	1.3
50.96	8.754×10^{-8}	1.3	1.5	41.08	2.047×10^{-5}	1.1	1.3
51.40	8.597×10^{-8}	1.4	1.0	41.54	1.685×10^{-5}	1.1	1.3
51.85	9.385×10^{-8}	1.4	1.4	41.97	1.367×10^{-5}	1.0	1.3
52.31	1.094×10^{-7}	1.4	1.6	42.42	1.117×10^{-5}	1.2	1.4
52.76	1.309×10^{-7}	1.3	1.5	42.87	8.627×10^{-6}	1.3	1.4
53.19	1.545×10^{-7}	1.4	1.3	43.33	6.939×10^{-6}	1.4	1.5
53.65	1.771×10^{-7}	1.3	1.3	43.77	5.537×10^{-6}	1.4	1.5
54.11	2.071×10^{-7}	1.2	1.2	44.46	3.790×10^{-6}	1.7	1.6
54.56	2.278×10^{-7}	1.1	1.0	52.08	1.726×10^{-7}	2.1	1.3
55.00	2.560×10^{-7}	1.4	0.9	52.77	2.187×10^{-7}	1.8	1.1
55.45	2.762×10^{-7}	1.3	0.8	53.22	2.444×10^{-7}	1.6	1.0
55.91	2.932×10^{-7}	1.3	0.8	53.67	2.641×10^{-7}	1.5	0.9
56.36	3.105×10^{-7}	1.0	0.7	54.13	2.956×10^{-7}	1.4	0.8
56.80	3.274×10^{-7}	1.0	0.6	54.57	3.177×10^{-7}	0.9	0.7
57.25	3.312×10^{-7}	1.0	0.5	55.02	3.303×10^{-7}	0.9	0.7
57.70	3.453×10^{-7}	1.0	0.5	55.48	3.468×10^{-7}	0.8	0.6
58.17	3.483×10^{-7}	1.0	0.5	55.93	3.547×10^{-7}	0.8	0.6
58.61	3.496×10^{-7}	1.1	0.4	56.37	3.666×10^{-7}	0.6	0.5
59.07	3.532×10^{-7}	1.1	0.4	56.81	3.651×10^{-7}	0.6	0.5
59.53	3.540×10^{-7}	1.2	0.4	57.27	3.746×10^{-7}	0.6	0.5
60.00	3.530×10^{-7}	1.3	0.4	57.73	3.814×10^{-7}	0.6	0.4
				58.17	3.763×10^{-7}	0.5	0.4
				58.62	3.728×10^{-7}	0.6	0.4
				59.07	3.690×10^{-7}	0.6	0.4
				59.53	3.635×10^{-7}	0.6	0.4
				59.99	3.548×10^{-7}	0.6	0.4
				60.66	3.394×10^{-7}	0.6	0.5
				61.58	3.228×10^{-7}	0.7	0.5

TABLE VI. *(Continued).*

θ (deg)	$d\sigma/d\Omega$ (fm^2/sr)	Uncertainty Statistical (%)	Uncertainty Systematic (%)
	$E_0 = 431$ MeV		
40.27	2.736×10^{-5}	1.2	1.8
40.73	2.216×10^{-5}	1.2	1.8
41.19	1.832×10^{-5}	1.2	1.8
41.64	1.473×10^{-5}	1.3	1.8
42.08	1.194×10^{-5}	0.9	1.9
42.54	9.495×10^{-6}	1.0	1.9
43.00	7.501×10^{-6}	1.0	1.9
43.46	5.956×10^{-6}	1.1	2.0
43.92	4.557×10^{-6}	1.1	2.0
44.36	3.590×10^{-6}	1.6	2.1
44.84	2.625×10^{-6}	1.1	2.1
45.30	1.953×10^{-6}	1.2	2.2
45.76	1.442×10^{-6}	1.3	2.2
46.24	1.021×10^{-6}	1.8	2.2
46.70	7.136×10^{-7}	2.0	2.3
47.16	5.102×10^{-7}	2.1	2.4
47.59	3.486×10^{-7}	1.6	2.4
48.05	2.374×10^{-7}	1.6	2.4
48.51	1.623×10^{-7}	1.6	2.3
48.94	1.159×10^{-7}	1.9	1.9
49.40	9.512×10^{-8}	1.4	1.3
49.86	9.072×10^{-8}	1.3	1.0
50.24	9.928×10^{-8}	1.2	1.2
50.70	1.147×10^{-7}	1.2	1.4
51.16	1.373×10^{-7}	1.2	1.4
51.54	1.662×10^{-7}	1.7	1.2
52.00	1.918×10^{-7}	1.5	1.1
52.46	2.171×10^{-7}	1.4	1.0
52.84	2.386×10^{-7}	1.1	0.9
53.30	2.732×10^{-7}	1.0	0.8
53.76	2.908×10^{-7}	1.0	0.8
54.14	3.180×10^{-7}	1.3	0.6
54.60	3.320×10^{-7}	1.3	0.6
55.16	3.535×10^{-7}	1.1	0.5
55.63	3.617×10^{-7}	1.0	0.5
56.08	3.730×10^{-7}	1.0	0.5
56.53	3.748×10^{-7}	1.1	0.4
57.08	3.747×10^{-7}	1.3	0.4
57.54	3.838×10^{-7}	1.2	0.4
58.00	3.816×10^{-7}	1.2	0.4
58.46	3.849×10^{-7}	1.2	0.4
58.90	3.745×10^{-7}	1.1	0.4
59.34	3.672×10^{-7}	1.2	0.4
59.80	3.535×10^{-7}	1.2	0.4
60.26	3.490×10^{-7}	1.3	0.4
60.72	3.340×10^{-7}	1.4	0.4
61.16	3.294×10^{-7}	1.7	0.4
61.62	3.073×10^{-7}	1.8	0.5
62.08	3.043×10^{-7}	2.0	0.5
62.53	2.804×10^{-7}	2.3	0.5

The ground-state charge density was deduced from the experimental cross sections in a so-called "model-independent" analysis. Constraints imposed by the assumption of a phenomenological model are minimized in such an analysis by parametrizing the ground-state charge distribution $\rho(r)$ with a complete set of zeroth-order Bessel functions of the first kind [29]:

$$\rho(r) = \begin{cases} \sum_{\nu=1}^{\infty} a_\nu j_0(q_\nu r) , & r \le R , \\ 0 , & r > R . \end{cases} \tag{5}$$

Here R is the cutoff radius of the charge distribution, and $q_\nu R$ is the νth zero of the Bessel function: $q_\nu = \nu\pi/R$.

In the first Born approximation the expansion coefficient a_ν is related to the form factor at q_ν through the expression, $a_\nu = q_\nu^2 F_0(q_\nu)/2\pi R$. The form factor squared F_0^2 is defined as σ/σ_M, where σ_M is the Mott cross section [28]. The normalization of the charge distribution imposes the constraint

$$ZF_0(q=0) = 4\pi \int_0^\infty \rho(r) r^2 dr = \sum_{\nu=1}^{\infty} (-1)^{\nu+1} \frac{4\pi R}{q_\nu^2} a_\nu .$$

TABLE VII. Error Sources.

Parameter	Statistical	Systematic
Scattering angle ($\Delta\Theta$)	<0.03°	0.015°
Incident energy ($\Delta E/E$)	<0.04%	0.08%
Radiative correction		<0.3%
Efficiency	0.5%	
Dead-time correction		<0.5%
QDQ monitor	<0.1%	
QDD stability	<0.5%	
Count-rate response of bin	<0.5%	
Bin-width correction		<0.2%

TABLE VIII. Uncertainties in the absolute normalization of the NIKHEF-K data. The systematic errors are divided in two categories: $\sigma_{\rm I}$, which change the normalization of all cross sections in the same direction; and $\sigma_{\rm II}$, which can change the normalization in either direction.

Measurement	$\sigma_{\rm I}$ (%)	$\sigma_{\rm II}$ (%)
Charge integrator	0.1	
Solid angle		
beam geometry		0.5
quadrupole field	1.0	
Target thickness		
target angle ($\Delta\theta_{\rm target} = 0.3°$)	0.3	
average thickness	0.3	
Incident energy ($\Delta E/E = 0.08\%$)		0.3
Scattering angle ($\Delta\Theta = 0.015°$)		0.2
Detection efficiency	0.5	
Radiative correction	0.1	0.3
Dead-time correction		0.5
Total uncertainty	2.3[a]	0.8[b]

[a] Linear sum.

[b] Quadratic sum.

If the data set is limited to a maximum momentum transfer, q_{max}, only the coefficients a_ν for $\nu \leq q_{max}R/\pi$ are determined. As suggested by Dreher *et al.* [29] the data set was extrapolated to higher momentum transfer by expressing the asymptotic behavior of $F_0(q)$ in terms of the folded proton form factor [30]:

$$F_0^{asymp}(q) \sim \frac{F_p(q)}{q^4} ,$$

where $F_p(q)$ is the proton form factor:

$$F_p(q) = e^{-q^2\langle r^2\rangle/6} ,$$
$$\langle r^2\rangle^{1/2} = 0.86 \text{ fm}.$$

This extrapolation was incorporated into the fit by simulating the form factor from q_{max} to $2q_{max}$ with pseudodata [29, 31]:

$$F_0(q_\nu) = 0 \quad q_{max} < q \leq 2q_{max} ,$$

with

$$\Delta^2 F_0(q_\nu) = \tfrac{1}{3}[F_0^{asymp}(q_\nu)]^2 .$$

The direct relation between the expansion coefficients a_ν and the form-factor value $F_0(q_\nu)$ facilitates the estimate of the so-called incompleteness error, which is traditionally defined as the error due to the absence of data at q values larger than q_{max}.

Since the choice of the cutoff radius R introduces some model dependence, the influence of R on the charge distribution has been studied. The optimum number of terms in the Fourier-Bessel series for different values of R was obtained from the formula: $\nu_{max} = 2q_{max}R/\pi$. The cutoff radius R was varied between 5 and 12 fm in a combined analysis of our measurements with data from earlier measurements [8, 9, 32, 33]. It was found that the fit deteriorated rapidly for $R < 6$ fm, while the description of the data sets hardly changed for $6 < R < 10$ fm (see Fig. 9). A value of 8 fm was chosen based on the F test [34] for the significance of additional terms describing the charge density.

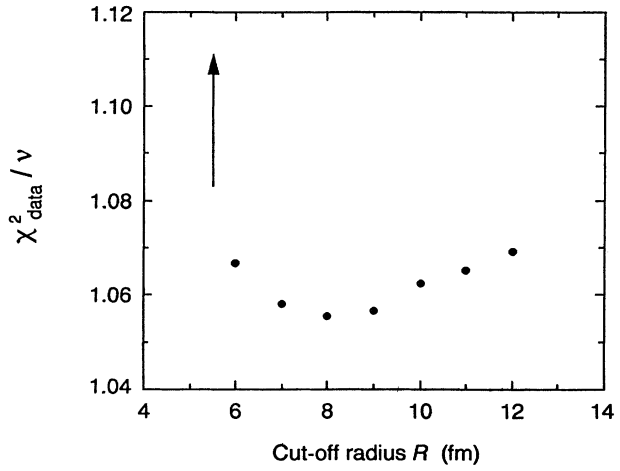

FIG. 9. The overall goodness of fit per degree of freedom χ^2/ν as a function of R, the cutoff radius.

B. Results of the static analysis

The q_{eff} range of the NIKHEF-K data is limited to 1.0–2.3 fm^{-1}. In order to obtain a static charge density that describes the NIKHEF-K data at one energy, additional measurements over lower and similar momentum transfers have been included. The data sets used are listed in Table IX. The energy ranges of the data from the Instituut voor Kernfysisch Onderzoek (IKO) [33] ($20< E_0 <80$ MeV), the National Bureau of Standards (NBS) [32] ($24< E_0 <116$ MeV) and the University of Mainz [9] ($100< E_0 <320$ MeV) have the largest overlap with the low-energy data set of NIKHEF-K. Therefore, the best-fit charge density was determined from these data sets and the NIKHEF-K low-energy data sets at 238 and 243 MeV (run II and IV, see Table II). The IKO and NBS data sets consist of absolute cross sections

TABLE IX. A tabulation of the results of three different fits to the data using a Fourier-Bessel parametrization of the ground-state charge density. The data points in the region of the minimum were omitted in all fits. In the first fit only the normalization factor of each data set was varied. In the second fit the normalization was varied and the momentum scales of the Mainz and Stanford data were recalibrated. In the third fit the cross section values were corrected for dispersive contributions before the analysis. The normalization factor for a data set is defined as norm = $\sigma_{fit}/\sigma_{exp}$. Only statistical errors are given.

				Fit 1 Nominal values		Fit 2 E_0 calibration varied			Fit 3 E_0 calibration varied and dispersion corrections		
Data (No. points)		q_{eff} (fm^{-1})	E_0 (MeV)	Norm	χ^2	Norm	ΔE_0 (%)	χ^2	Norm	ΔE_0 (%)	χ^2
IKO [33]	(9)	0.2–0.7	20–80	0.992(3)	5.7	0.993(3)	0.0	5.4	0.994(3)	0.0	5.0
NBS [32]	(35)	0.1–1.0	24–116	0.997(1)	34.0	0.998(1)	0.0	33.7	0.999(1)	0.0	34.7
Mainz [9]	(16)	0.3–0.7	100–300	0.995(2)	15.1	0.996(2)	0.0	14.0	0.996(2)	0.0	14.4
Mainz [9]	(27)	0.5–1.4	150.24	1.003(2)	20.6	1.015(4)	−0.25(6)	14.1	1.012(4)	−0.22(6)	16.0
	(8)	1.1–2.0	240.17	0.965(3)	25.7	0.980(7)	−0.22(4)	9.0	0.978(7)	−0.22(4)	6.4
	(16)	1.3–2.7	300.52	1.005(4)	35.7	1.015(6)	−0.18(3)	15.5	1.015(6)	−0.20(3)	17.8
	(8)	1.4–2.3	320.10	1.077(4)	8.0	1.074(6)	−0.09(2)	2.6	1.072(6)	−0.10(3)	2.9
Stanford [8]	(23)	1.1–2.8	374.50	0.993(8)	14.9	0.997(10)	-0.18(7)	8.1	0.992(10)	−0.19(7)	8.9
	(16)	2.1–4.0	747.20	1.017(14)	7.0	1.011(15)	−0.05(6)	6.6	0.995(15)	−0.07(9)	7.9
This work	(43)	1.0–2.0	240.00	1.009(3)	75.5	0.999(4)	0.0	67.5	0.995(4)	0.0	60.4
This work	(74)	1.1–2.3	430.00		118.5		0.0	89.5		0.0	90.1
$\sum\chi^2/\nu$					360.6/252			280.2/252			279.0/252

in the q_{eff} range 0.2–0.8 fm^{-1} and 0.1–1.0 fm^{-1}, respectively. The Mainz data consist of five separate sets with overlapping momentum-transfer ranges $0.3< q_{\text{eff}} <2.7$ fm^{-1}. The Mainz data set in the q_{eff} range $0.3< q_{\text{eff}} <0.7$ fm^{-1} has an absolute normalization, while the normalization factors of the other four sets must be determined in a fit in conjunction with absolute data. The normalizations of the absolute data sets were fixed in this part of the analysis to minimize absorption of a possible energy dependence of the form factor into the fit.

The original (raw) Mainz data were reanalyzed using the same procedure described above for the NIKHEF-K data so that the final cross-section corrections to the Mainz data for solid-angle effects and energy spread were consistent with the best-fit density obtained from the combined analysis of all the data; the changes in the Mainz cross sections due to this procedure were very small. The fitting of the combined data sets was performed using a version of the code MEFIT [25] modified to incorporate the corrections for finite solid angle and energy spread described above. The energy of the Mainz data was adjusted slightly in a manner similar to the fits described in the next section.

As was pointed out in the description of the data reduction, the relative normalization of the NIKHEF-K data sets at low and high energy is well established. In the analysis discussed in this section, the normalization of the NIKHEF-K data was determined by fitting the two low-energy sets in conjunction with the absolute data. In this fit ($\chi^2/\nu=163.8/148$) all cross sections in the region of the diffraction minimum ($1.6< q_{\text{eff}} <1.95$ fm^{-1}) were excluded, so that deviations in the region of the minimum would not be absorbed into the normalization factor. A more detailed study of the absolute normalization factor of the complete NIKHEF-K data set will be presented in Sec. V.

In a second fit the low-energy NIKHEF-K data in the minimum were included, but the absolute normalization of the data was fixed at the value obtained from the first fit. Data from the experiment of Reuter *et al.* [9] taken in the region of the diffraction minimum were omitted from this fit because they were replaced by the higher-quality data from the present experiment. In this way we deduced a charge distribution that describes the form-factor minimum at the lower energy of the present experiment as well as possible. It should be noted that the cross section in the diffraction minimum comes mainly from Coulomb distortion effects whose magnitude is determined by the complete charge distribution and thus mainly by the cross-section values outside the minimum. The overall quality of the fit is reasonable ($\chi^2/\nu=244.3/174$, with the 25 data points in the minimum contributing 61.8). The percentage deviations of the measured cross sections from the predictions of the best-fit charge density are plotted as a function of q_{eff} in Fig. 10 and the top part of Fig. 11(a) for the IKO, NBS, Mainz and low-energy NIKHEF-K data; the agreement between experiment and the predictions of the best-fit density is good. However, in the momentum-transfer range $1.2< q_{\text{eff}} <1.6$ fm^{-1} the NIKHEF-K data appear to be systematically about 1% lower than the fit, and a

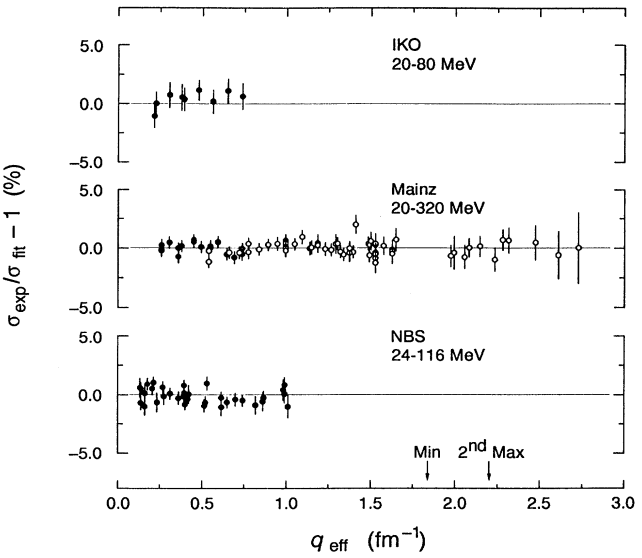

FIG. 10. The percentage deviation between predictions of the best-fit charge density and cross section values of IKO [33], Mainz [9], and NBS [32] as a function of the effective momentum transfer q_{eff}. The position of the minimum and of the second maximum of the form factor are indicated. Absolute cross sections are represented in the figure by closed circles (•) and relative cross sections by open circles (o).

3(1)% deviation between experiment and best fit is apparent in the first diffraction minimum at $q_{\text{eff}}=1.84$ fm^{-1}.

The best-fit static charge density inferred from this procedure can now be used to predict the cross-section values for the high-energy NIKHEF-K data sets (runs I, III, and V), and for data measured in a subsequent experiment [35] at MIT-Bates at 690 MeV. The absolute normalization of the MIT-Bates data (0.90) was determined by comparing data on the 2^+ level measured simultaneously with the predictions of the transition density that provided a fit to our measurements and earlier data on this state. The percentage deviations between the experimental values and predictions are shown in Figs. 11(b) and (c). Systematic uncertainties were estimated by repeating the analysis with the NIKHEF-K and MIT-Bates cross-section values increased and decreased by their systematic errors independently for the low- and high-energy data. The influence of these systematic effects on the deviation between experiment and prediction is indicated by the shaded area in Fig. 11. This figure shows an unambiguous energy dependence of the form factor. At the higher energies the cross section in the region of the diffraction minimum is increased relative to the prediction of a static-analysis fit to the lower-energy data sets by as much as 8(1)% at 430 MeV and 18(3)% at 690 MeV. Furthermore, the cross section drops below the predicted values on both sides of the minimum for the 430-MeV data set and on one side for the 690-MeV data set.

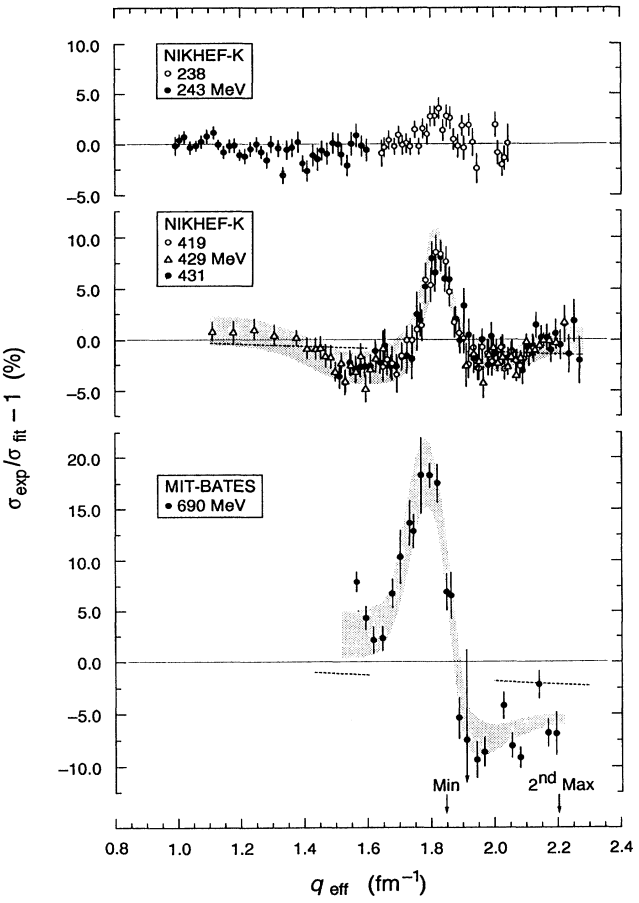

FIG. 11. The differences between the cross sections measured at six incident electron energies (from 238 to 690 MeV) and the values predicted by the ground-state charge density parameters obtained from the data at lower energies (see text). The dashed curves indicate the energy dependence of the dispersive contribution according to Friar and Rosen [12] between 240 MeV and the energy under consideration.

C. Comparison with other measurements

As was mentioned earlier, measurements from Mainz [9] and Stanford [8] include data in the region of the diffraction minimum. A comparison of these data with the predictions of our best-fit charge density, which was obtained by fitting low-energy data of IKO, Mainz, NBS, and NIKHEF-K, supplies further information on the energy dependence of the dispersion correction in the minimum.

In contrast to the high-energy NIKHEF-K and MIT-Bates cross sections, the normalization of the Mainz and Stanford data relative to the low-energy NIKHEF-K data is not known precisely. Normalization factors for the Mainz data were determined as described in the preceding section by a combined fit of all data outside the minimum; the normalization of the Stanford data was obtained by comparing the cross sections measured at Stanford outside $1.6 < q_{\text{eff}} < 1.95$ fm^{-1} with the values predicted by the best-fit charge density. This procedure introduces an uncertainty in the deviation from the low-energy prediction because the average deviation outside the minimum is absorbed in the normalization factors. It should be noted that the unfolding corrections for the effects of finite solid angle and straggling in the target amounted to 12% near the form-factor minimum for the Mainz and Stanford data sets; the information about the Stanford data required to correct for finite-solid-angle and target straggling effects was taken from Friar and Negele [36].

The percentage deviations of the data sets of Mainz and of Stanford from the predictions of the charge density that provided a best-fit to the low-energy data are plotted in Fig. 12 as a function of q_{eff}. The form-factor minimum was shifted to the same momentum-transfer value as was observed in the more precise NIKHEF-K data by adjusting the incident energy of the different Mainz data sets by between 0.08% and 0.25% and of the Stanford data by 0.18%. However, it is important to note that deviations observed in the diffraction minimum between these data sets and the predictions of our best-fit static charge density cannot be removed by *any* adjustment of energy or normalization. Figure 13 summarizes the deviations observed in the diffraction minimum as a function of beam energy; the discrepancy increases with incident energy.

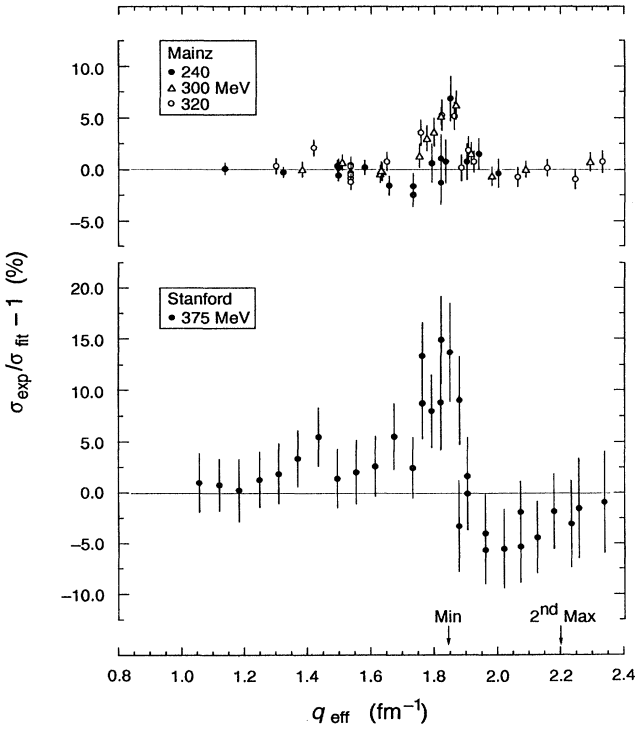

FIG. 12. The percent deviations of the cross sections measured at Mainz [9] and Stanford [8] in the region of the form-factor minimum from the predictions of our best-fit charge density as a function of q_{eff}.

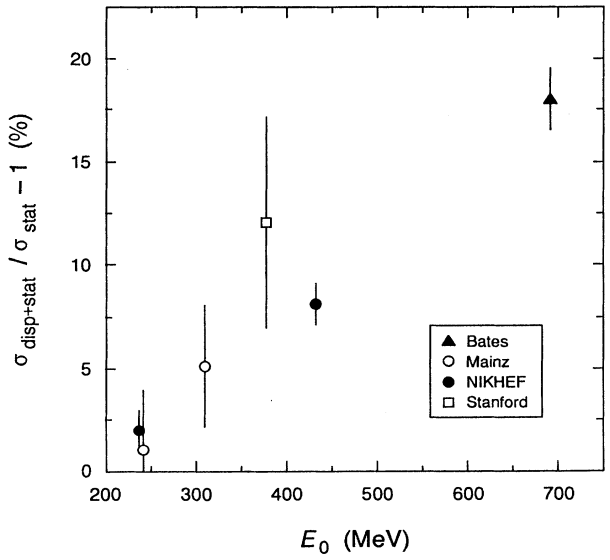

FIG. 13. The energy dependence of the "filling in" of the form-factor minimum.

D. Interpretation in terms of dispersive effects

If higher-order contributions to the static analysis are negligible, the static charge density deduced from lower-energy data should accurately predict the cross sections at other incident energies over the same momentum transfer. Figure 11 shows clearly that the elastic form factor exhibits an energy dependence. The two most important corrections to the standard static analysis are given by the dispersion and recoil corrections. Dispersion corrections have been discussed briefly in the introduction; they are expected to show a significant energy dependence [12, 37, 38]. The recoil correction arises from the interaction of the electron with the current associated with the recoiling nucleus. Calculations [39, 40] of the recoil correction, performed within the Breit approximation, suggest that the correction is at most $\pm 1\%$ in the region of the first diffraction minimum of ^{12}C. Furthermore, the calculated recoil correction depends very little on the incident energy. Therefore, it seems reasonable to interpret the observed energy dependence of the ^{12}C form factor in terms of dispersive processes only.

A general feature of available theoretical calculations of the dispersion correction is a smooth increase in the correction outside diffraction minima with increasing momentum transfer. The small deviations of the low-energy data outside the minimum relative to the predictions of the best-fit density [see Fig. 11(a)] suggest that this smooth part of the dispersive contribution at this energy (if indeed it is present) has been absorbed into the static charge density. The discrepancy observed in the low-energy data in the minimum between experiment and fit is then the local surplus of dispersive contributions above this smooth function. In fact, any comparison between experiment and the predictions of this best-fit charge density will show the size of dispersive effects relative to this smooth dispersive contribution at about 240 MeV.

Some general features of dispersive contributions in ^{12}C can be extracted from the measurements. Since the first Born amplitude and the real part of the Coulomb-distortion amplitude f_C change sign (and therefore go through zero) in the minimum of the form factor, the leading dispersive contribution in the minimum is given by the product of the imaginary part of f_C and the dispersion amplitude f_D. The contribution coming from f_D^2 is much smaller since f_C comes from a coherent sum of the different proton contributions in the nucleus while f_D turns out to be an incoherent sum [12]. Therefore, the linear energy dependence of the deviation observed in the minimum and the $1/E_0$ dependence of f_C in the minimum [1] lead to the conclusion that $\mathrm{Im}(f_D)$ has an energy dependence in the minimum given by $c_1 + c_2/E_0$.

If one assumes that the E_0 dependence is monotonic and does not change sign, two different classes of dispersion corrections are compatible with the observed energy dependence outside the minimum. Two extreme cases of each class are illustrated schematically in Fig. 14. The two classes are distinguished by the fact that the dispersion correction can become negative and increase in absolute magnitude with energy for one group [see Fig. 14(a)] while it is positive and decreases with energy for the other group [Fig. 14(b)]. The corrections have been extended to zero momentum transfer through the use of unitarity and dispersion relations [41, 42]. These model-independent ingredients prescribe that the dispersion amplitude is finite and has positive real and imaginary parts for $q = 0$, so the dispersion correction at $q = 0$

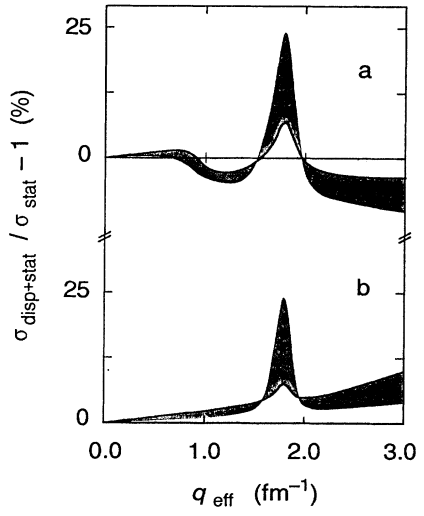

FIG. 14. Schematic representations of different types of dispersion corrections that are compatible with the observed energy dependence of the form factor. The thick solid curve indicates the correction for low energy while the thin curve shows the correction for high energy. The shaded area displays the energy dependence.

is zero and its derivative with respect to q is positive.

We have compared the observed energy dependence with the dispersion-correction calculations of Friar and Rosen [12]. As can be seen in Fig. 15, their calculations agree qualitatively with the second class of dispersion corrections, discussed above. They predict a strongly peaked effect in the diffraction minimum and an energy dependence on both sides of the minimum that has the opposite sign of the correction in the minimum and decreases as $1/E_0$. The agreement between the predictions of this calculation and our experiment in the region of the minimum is poor. First, the observed effect is nearly an order of magnitude larger than the calculation. Second, the observed effect increases roughly linearly with energy while the calculated effect is almost independent of the beam energy. One explanation of this discrepancy is that the imaginary part of the calculated dispersion amplitude is grossly underestimated since this part of the amplitude dominates near the diffraction minimum (where the real part changes sign). The discrepancy between theory and experiment in the minimum does not necessarily have implications for the validity of the calculated dispersion amplitude outside the minimum. A number of approximations have been made by Friar and Rosen, and there are several possibilities for modifying the imaginary part of the dispersion amplitude, such as the inclusion of the transverse part of the dispersion amplitude [36]. The precise nature of the changes in the theory that are required to match our measurements is beyond the scope of the present work.

The energy dependence of the dispersive contribution outside the minimum as calculated by Friar and Rosen is indicated in Fig. 11 by dashed curves. These curves were obtained by parametrizing their results for 375 and 747 MeV (shown in Fig. 15) as a function of E_0 and q^2 with a polynomial outside the region of the first diffraction minimum:

$$\sigma_{\text{stat+disp}} = \sigma_{\text{stat}} \left(1 + \frac{1.1q^2 + 0.1q^4}{E_0}\right) , \tag{6}$$

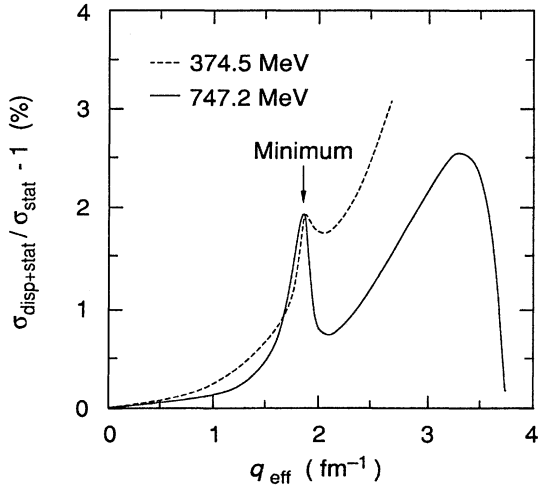

FIG. 15. The results of the calculations of Friar and Rosen [12] for dispersion corrections to elastic scattering from ^{12}C at 374.5 and 750 MeV.

where $\sigma_{\text{stat+disp}}$ is the dynamic cross section, which includes dispersive contributions, and σ_{stat} is the static cross section. Their prediction for the energy dependence outside the minimum agrees reasonably well with the measurements at 430 MeV, but differences are apparent at 690 MeV. We conclude that although the real part of the calculated dispersion amplitude is roughly compatible with the measurements at 430 MeV, the disagreement with the 690 MeV measurements seems to indicate that the energy dependence of the real part of the dispersion amplitude is not correct either.

V. THE EFFECTS OF DISPERSION CORRECTIONS ON THE INFERRED ^{12}C GROUND-STATE CHARGE DISTRIBUTION

We have investigated the influence of dispersive effects on the extracted ground-state charge distribution by incorporating the dispersion corrections calculated by Friar and Rosen [12] in an analysis of all available data on elastic electron scattering from ^{12}C. Although the energy dependence we observed in the region of the form-factor minimum ($1.6 < q_{\text{eff}} < 1.95$ fm^{-1}) is an order of magnitude larger than the predictions of Friar and Rosen, their calculations are reasonably compatible with the energy dependence observed outside the minimum. In order to avoid ambiguities from the large discrepancy in the region of the minimum, all cross-section data points in this region were omitted in the analysis. This procedure still yields an accurate estimate of the charge distribution for ^{12}C because the cross section in the minimum is strongly correlated with the cross section outside that region by the Coulomb corrections.

A. Fourier-Bessel analysis results

The present data were analyzed in conjunction with the data of IKO [33], Mainz [9], NBS [32], and Stanford [8]; a total of 275 data points were available, covering a q_{eff} range $0.1 < q_{\text{eff}} < 4.0$ fm^{-1}. As has been discussed above, all data in the region of the first diffraction minimum ($1.6 < q_{\text{eff}} < 1.95$ fm^{-1}) were excluded from the analysis.

The best-fit charge density was deduced from the combined data set in a χ^2 analysis with the phase-shift program MEFIT [25] using a Fourier-Bessel parametrization for the ground-state charge density. Possible discrepancies in the normalizations and momentum-transfer scales of the different data sets were resolved before applying dispersion corrections. A total of three fits were performed; the results of these fits are presented in Table IX and are discussed, in turn, below.

In the first fit the normalization of each data set, including the absolute data sets, was permitted to vary, constrained only by the overall normalization of the charge distribution. The relative normalizations of the NIKHEF-K data sets were coupled through the analysis described in Sec. III. The overall quality of the fit (Table IX, column 1) is reasonable ($\chi^2/\nu = 360.6/252$). The change in the normalization factor for the absolute NBS data is within the estimated 0.37% uncertainty [32], that

for the absolute Mainz data is just outside its estimated 0.4% uncertainty [9], while the IKO normalization factor has changed by an amount that is three times its estimated 0.24% uncertainty [33].

The χ^2 per point for the Mainz and NIKHEF-K data sets above q=1 fm^{-1} is larger than those of the other sets. A comparison of the data in the minimum—which were not included in the fit—revealed that the form-factor minimum in these data sets occurs at different $q_{\rm eff}$ values. It is quite likely that this is the result of errors in the absolute energy calibrations of the experiments. The position of the minimum as described by the Stanford data also does not coincide with the fit, although this is not apparent from the χ^2 values for these data. To investigate the energy calibration of these high-q data sets, we performed a second fit in which the incident energies of the Mainz data above $q_{\rm eff}$=1 fm and Stanford data were varied relative to their nominal values. The NIKHEF-K energies were fixed in this fit and the energy of the absolute Mainz data was not varied since recalibration of the incident energy is strongly correlated to the normalization factor at low q values.

Variation of these energies results in a substantial improvement in the quality of the fit (Table IX, column 2; the χ^2/ν value drops from 1.43 to 1.11). The positions of the minima as described by the cross section values of various data sets coincide after the recalibration of the momentum-transfer scale. The incident energies of the Mainz data determined by this fit show small, systematic deviations of about 0.09 to 0.25% from their original values; for the Stanford data the fit resulted in a 0.18(7)% energy change. In both cases the deviations are somewhat larger than the systematic errors quoted by the authors, 0.12% and 0.1%, respectively.

The use of the NIKHEF-K data sets as a reference for the recalibration of the momentum scale above $q_{\rm eff}$=1 fm^{-1} is justified by the energy-calibration method used at NIKHEF-K, which is considered to be more accurate than the methods used in the Mainz and Stanford experiments. Our method consists of measuring the recoil-energy differences and excitation spectra for different nuclei along the focal plane (see Sec. II B). The incident energy and the spectrometer constants were calibrated in a single, consistent framework using measurements performed during the actual data taking. In the calibration procedures of the other two laboratories either the incident energy (Stanford) or the spectrometer constants (Mainz) were determined separately from the ^{12}C measurements. This can introduce systematic errors in the energy calibration. The energy-calibration procedure used for the NIKHEF-K data has been checked by varying the low-energy and high-energy calibrations in two separate fits. The differences between the energies obtained by this procedure and that of our absolute calibration were well within the estimated systematic error of 0.08%.

The charge density distribution inferred from this second fit in which the energies of the Mainz and Stanford high-q data were varied was used as a reference for the study of the influence of dispersive effects. First, all cross sections were "corrected" for dispersive contributions using the theory of Friar and Rosen [12] and the parametrization of Sec. IV D. Then, a third fit was performed in which the normalizations and incident energies were again treated as free parameters. Although the dispersion correction used is based on a closure approximation and therefore less reliable at low incident energies, we applied this correction to the IKO and NBS data as well; the correction is very small (<0.2%) at the momentum transfers of these data. The validity of the correction for the high-q Stanford data at 747 MeV is also questionable because Friar and Rosen [12] used a two-proton correlation function, calculated in the harmonic-oscillator shell model, which is not expected to provide a good description for high-q data. However, the statistical uncertainties in these data are much larger than the corrections applied (<2.5%).

The correction for dispersive contributions does not improve the total χ^2 (Table IX, column 3) of the fit significantly, but it does result in small changes in the χ^2 values of individual data sets. Since the dispersion corrections contribute most to low-energy data sets measured at relatively high q (NIKHEF-K and Mainz data at E_0 = 240 MeV), it may be significant that their χ^2 values improve slightly while the χ^2 values of the other data sets increase.

The fit results given in columns 2 and 3 of Table IX indicate that the normalization factor for the NIKHEF-K data is 0.999(4) and 0.995(4), respectively. Taking the average of these values and adding the total systematic error of 2.4% (see Table VIII) quadratically yields an absolute normalization factor for the NIKHEF-K data sets of

$$\text{norm}_{\text{NIKHEF-K}} = 0.997 \pm 0.025 \ .$$

This value supports the normalization presented in Sec. III E, which was determined independently from the fits to the data.

B. Ground-state charge distribution

The coefficients, a_ν, describing the "reference" charge distribution (determined from the second fit, column 2 of Table IX) are listed in the second column of Table X. In the third column of this table the charge distribution coefficients that were extracted from the dispersion-corrected data sets are given; if the theoretical calculation of dispersive effects is correct, these represent the "true" charge density. The first nine coefficients in both sets were determined directly from the combined data sets ($q_{\rm max}$=4.0 fm^{-1}); the remaining coefficients were determined by the high-q assumptions discussed earlier. The changes in the expansion coefficients due to dispersion corrections increase with order ν. This is not surprising since the magnitude of the dispersion corrections increases with the momentum transfer, and the value of a_ν is determined by the form factor in the vicinity of $q_\nu = \nu\pi/R$.

The effect of dispersion corrections on the extracted charge distribution is shown in Fig. 16. The application of dispersion corrections shifts charge from the center of

TABLE X. The Fourier-Bessel coefficients a_ν determined from the fits. The values in the second column (without dispersion corrections) represent the parametrization of the reference charge distribution (fit 2, Table IX). The values in the third column were deduced from the analysis of the dispersion-corrected cross sections (fit 3, Table IX). The statistical errors in both sets of coefficients are given in the fourth column, and the change in the coefficients between the fits with and without the inclusion of dispersion corrections are listed in the last column. The rms radii of these charge distributions and their statistical errors are also given. The cutoff radius for the fits was at R=8 fm.

ν	Without dispersion corrections a_ν (fm^{-3})	With dispersion corrections a_ν (fm^{-3})	Error (%)	Δa_ν (%)
1	1.5721×10^{-2}	1.5709×10^{-2}	0.05	0.08
2	3.8723×10^{-2}	3.8610×10^{-2}	0.11	0.29
3	3.6616×10^{-2}	3.6418×10^{-2}	0.17	0.54
4	1.4390×10^{-2}	1.4293×10^{-2}	0.20	0.68
5	-4.5062×10^{-3}	-4.4628×10^{-3}	0.25	0.97
6	-9.9771×10^{-3}	-9.8420×10^{-3}	0.28	-1.37
7	-6.7970×10^{-3}	-6.6518×10^{-3}	0.77	-2.18
8	-2.7632×10^{-3}	-2.7066×10^{-3}	1.96	-2.09
9	-5.8502×10^{-4}	-5.6697×10^{-4}	7.68	-3.18
10	-2.6986×10^{-4}	-2.7453×10^{-4}		
11	-1.8522×10^{-4}	-1.7093×10^{-4}		
12	1.0510×10^{-4}	1.2433×10^{-4}		
13	-3.8843×10^{-5}	-4.8496×10^{-5}		
14	1.2243×10^{-5}	1.5675×10^{-5}		
15	-3.4788×10^{-6}	-4.5194×10^{-6}		
16	9.0889×10^{-7}	1.1920×10^{-6}		
17	-2.2015×10^{-7}	-2.9065×10^{-7}		
18	4.9631×10^{-8}	6.5845×10^{-8}		
$\langle r^2\rangle^{1/2}$ (fm)	2.4711(55)	2.4776(55)		

the nucleus to the edge, in qualitative agreement with the results of a similar analysis of a more restricted data set by Friar and Negele [36]. In that analysis, which also used the calculation of Friar and Rosen [12], the effect of dispersion corrections on the charge distribution was only half that found in the present analysis. However,

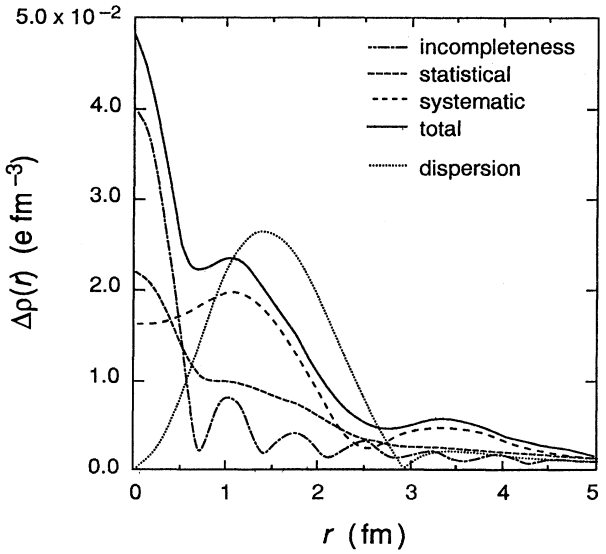

FIG. 16. The influence of dispersion corrections on the reference charge distribution. The statistical and incompleteness error and the uncertainties due to systematic errors in angle, incident energy, and normalization are also shown.

in Friar and Negele's analysis the dispersion corrections were treated as a systematic effect, and taken to be independent of other systematic uncertainties. In a fit in which dispersive contributions are neglected, some of the dispersive effects will be absorbed in both the inferred charge distribution and the concurrently determined normalization factors. To compensate for this feature of the uncorrected fit, the normalization factors should not be kept fixed, but allowed to vary when cross sections whose absolute normalizations are not known are corrected for dispersive contributions.

The normalization of the cross sections in our analysis of the combined data set was determined by the data with the highest accuracy, those of IKO, Mainz, and NBS, while the momentum scale was defined primarily by the data sets of NIKHEF-K and to a lesser extent by those of IKO and NBS. The influence of systematic errors in the normalization and the momentum scale was investigated by varying the parameters describing these data sets one at a time from their nominal values (fit 2, Table IX) to their systematic extremes. The systematic uncertainties in normalization, scattering angle, and incident energy are given in Table XI for each of the relevant data sets.

Figure 16 displays the uncertainties in the reference charge distribution due to the systematic errors in the momentum-transfer scale and in the normalization together with the statistical and incompleteness error. It is clear that for radii greater than 1 fm the uncertainty in the charge density comes mainly from systematic effects. The effect of dispersion corrections (as calculated

TABLE XI. Systematic uncertainties considered in the analysis.

Data	Norm (%)	$\Delta E/E$ (%)	$\Delta\theta$ (deg)
IKO	0.24	0.3	0.03
Mainz	0.4		
NBS	0.37	0.07	0.008
NIKHEF-K		0.08	0.015

by Friar and Rosen) on the inferred density is comparable to the effect of the experimental uncertainties.

C. rms charge radius

The rms radius of the charge density inferred from a static analysis of the data is 2.471 fm; it increases to 2.478 fm after dispersion corrections have been taken into account (see Table X). The statistical error in the rms radius is ±0.006 fm for both analyses; the systematic uncertainties are larger. Systematic variation of the normalization and the momentum-transfer scale results in a systematic error in the rms radius of ±0.007 fm. Calculations by Friar [42] in a Goldhaber-Teller model suggest that dispersion corrections cause changes in the rms radius ranging from 0.002 to 0.007 fm, depending on the approximations applied. This change in the rms radius is in agreement with that obtained from the present analysis.

The rms radius determined from the present work is listed in Table XII together with other recent results obtained from electron scattering and muonic x-ray experiments. The rms-radius values corrected for higher-order effects (i.e. for dispersive effects in electron scattering data and for nuclear polarization effects in muonic x-ray experiments) are also given where available. Our value for the RMS radius agrees, within uncertainties, with values obtained from earlier analyses of different data sets. The analyses by Reuter *et al.* [9] and by Sick [44] also estimated the influence of the dispersion corrections calculated by Friar and Rosen [12] on the rms radius. In both cases a smaller increase of the rms radius was reported: 0.004 fm by Reuter *et al.* [9]; and 0.002 fm by Sick [44]. Our analysis yields an increase of 0.007 fm. The smaller increase found by the Mainz group can be attributed to the fact that they fixed the normalization of the data sets to the values determined before the dispersion corrections were applied. The reason for the difference with the result of Sick [44] cannot be traced, because the details of his analysis are not presented.

Earlier comparisons [10] of rms radii determined by electron scattering and muonic x rays in the region of the Fe, Ni, and Zn isotopes indicated that the muonic-atom results were systematically higher by about 0.011(26) fm. A similar difference for ^{12}C was obtained by Ruckstuhl *et al.* [11] who reported a difference of 0.0124(53) fm relative to the ^{12}C rms radius determined from earlier electron scattering experiments in ^{12}C. The average ^{12}C rms radius inferred from the muonic-atom data presented in Table XII is 2.4827(19) fm; this value is in perfect agreement with the dispersion-corrected rms charge radius determined in this work from electron-scattering data. We find

$$\langle r^2\rangle_\mu^{1/2} - \langle r^2\rangle_e^{1/2} = 0.005 \pm 0.009 \text{ fm} .$$

This agreement suggests that the deviations reported earlier are probably due to either the neglect or the underestimation of the effect of dispersive contributions on the rms radius derived from electron-scattering data in previous analyses.

VI. CONCLUSIONS

The study of elastic electron-scattering cross sections from ^{12}C in a static analysis demonstrates the existence of a form-factor energy dependence. This energy dependence increases smoothly as a function of momentum transfer and incident energy in the region covered by the experiments ($1.0< q_{\text{eff}} <2.3$ fm^{-1}, $240< E_0 <690$ MeV). Outside the first diffraction minimum the discrepancy between the form factors deduced from data obtained at different energies can be as large as 5%; in the minimum

TABLE XII. rms charge radius of ^{12}C as determined from electron scattering and muonic atom experiments. THD=Technische Hochschule Darmstadt. SIN=Schweizerisches Institut für Nuklearforschung. ETH=Eidgenössische Technische Hochschule.

Method	Reference	Data	Without dispersion corrections $\langle r^2\rangle^{1/2}$ (fm)	With dispersion corrections $\langle r^2\rangle^{1/2}$ (fm)	$\delta\langle r^2\rangle^{1/2}$ (fm)
(e,e)	[31]	IKO+NBS+Stanford	2.472		0.015
(e,e)	[9]	Mainz	2.464	2.468	0.012
(e,e)	[42]	IKO+NBS+Stanford +THD	2.471	2.473	0.0055[a]
(e,e)	This work	IKO+Mainz+NBS +NIKHEF-K+Stanford	2.471	2.478	0.009
μ atom	[43]	Fribourg/SIN		2.472	0.015
μ atom	[11]	ETH/SIN		2.4829	0.0019

[a]Empirical information on the properties of nuclear wave functions at large radii is used to reduce the uncertainty in this analysis.

itself discrepancies as large as 18% have been observed.

This form-factor energy dependence has been interpreted in terms of dispersive effects which arise from virtual nuclear excitations in the scattering process. Comparison with the dispersion calculations of Friar and Rosen [12] shows fair agreement outside the diffraction minimum at lower energies. In a light nucleus such as ^{12}C the imaginary part of the dispersion amplitude has a minor contribution outside the diffraction minimum. This suggests that the size of the real part of the calculated dispersion amplitude is compatible with the experimental data but its energy dependence is not. In the minimum, however, the calculation is nearly an order of magnitude too small. This is probably due to an underestimate of the imaginary part of the dispersion amplitude, which dominates in ^{12}C only near the diffraction minimum. The imaginary part of the dispersion amplitude can be investigated further by performing measurements on a heavy nucleus where it is also enhanced outside the minimum through its interference with the Coulomb distortion amplitude; such a measurement on ^{208}Pb is underway at NIKHEF-K [45].

The energy dependence, size, and sign of the dispersion correction are well established in the minimum by measuring the form factor. However, neither the size nor sign of the correction outside the minimum can be deduced unambiguously from our measurements. Here, additional information from the comparison of elastic electron and positron scattering from ^{12}C will give a conclusive answer [46].

The discrepancies observed in the static analysis of the present data indicate that one should no longer neglect the effect of dispersive contributions in the analysis of high-precision elastic electron-scattering data. The effect of dispersive corrections on the ground-state charge distribution inferred from the ^{12}C(e,e) data is comparable to that of other experimental uncertainties. The rms charge radius of ^{12}C inferred from the electron scattering data increases by 0.007 to 2.478±0.009 fm when dispersion corrections as calculated by Friar and Rosen are included in the analysis. This RMS radius is in excellent agreement with the value from muonic x-ray studies; inclusion of dynamic corrections in the analysis of both (e,e) and muonic-atom data removes discrepancies reported earlier.

ACKNOWLEDGMENTS

We would like to thank Dr. J. L. Friar for helpful discussions on the interpretation of these data. This work is part of the research program of the Nationaal Instituut voor Kernfysica en Hoge Energie Fysica (NIKHEF, sectie K), which is financially supported by the Stichting voor Fundamenteel Onderzoek der Materie (FOM) and the Nederlandse Organisatie voor Wetenschappelijk Onderzoek (NWO). Additional support was provided by the U.S. National Science Foundation under Grant No. PHY–89–21146, and by the Bundesministerium für Forschung und Technologie, Bonn.

* Present address: Institut für Kernphysik der Johannes-Gutenberg-Universität, 65 Mainz, Germany.

† Present address: Ministerium des Innern Rheinland-Pfalz, 65 Mainz, Germany.

[1] T. de Forest, Jr., Phys. Lett. **32B**, 12 (1970).
[2] G. A. Peterson, J. F. Ziegler, and R. B. Clark, Phys. Lett. **17**, 320 (1965).
[3] D. W. Madsen, L. S. Cardman, J. R. Legg, E. F. Gundenheim, and C. K. Bockelman, Phys. Rev. Lett. **23**, 1122 (1969).
[4] J. F. Ziegler and G. A. Peterson, Phys. Rev. **165**, 1337 (1968).
[5] C. W. de Jager, R. Maas, and C. de Vries, Phys. Lett. **39B**, 188 (1972).
[6] L. S. Cardman, D. Kalinsky, J. R. Legg, R. Yen, and C. K. Bockelman, Nucl. Phys. **A216**, 285 (1973).
[7] R. Maas and C. W. de Jager, Phys. Lett. **48B**, 212 (1974).
[8] I. Sick and J. McCarthy, Nucl. Phys. **A150**, 631 (1970).
[9] W. Reuter, G. Fricke, K. Merle, and H. Miska, Phys. Rev. C **26**, 806 (1982).
[10] H. D. Wohlfahrt, Habilitationsschrift, University of Mainz (1976).
[11] W. Ruckstuhl, B. Aas, W. Beer, I. Beltrami, K. Bos, P. F. A. Goudsmit, H. J. Leisi, G. Strassner, and A. Vachi, Nucl. Phys. **A430**, 685 (1984).
[12] J. L. Friar and M. Rosen, Ann. Phys. (N.Y.) **87**, 289 (1974).
[13] C. de Vries, C. W. de Jager, L. Lapikás, G. Luijckx, R. Maas, H. de Vries, and P. K. A. de Witt Huberts, Nucl. Instrum. Methods **223**, 1 (1984).
[14] E. A. J. M. Offermann, C. W. de Jager, and H. de Vries, Nucl. Instrum. Methods **A262**, 298 (1987).
[15] H. Blok, E. A. J. M. Offermann, C. W. de Jager, and H. de Vries, Nucl. Instrum. Methods **262**, 291 (1987).
[16] F. Ajzenberg-Selove, Nucl. Phys. **A392**, 1 (1983).
[17] L. Landau, J. Phys. U.S.S.R. **8**, 201 (1944).
[18] L. W. Mo and Y. S. Tsai, Rev. Mod. Phys. **41**, 205 (1969).
[19] L. C. Maximon, Rev. Mod. Phys. **41**, 193 (1969).
[20] E. A. J. M. Offermann, Ph.D. thesis, University of Amsterdam (1988).
[21] H. A. Enge and S. R. Kowalski, Proceedings of the Third International Conference on Magnet Technology, Hamburg, 1970, edited by Committee MT3, Desy (A. Kurtze K.G. Hamburg, 1970), p. 366.
[22] H. G. Andresen, M. Müller, H. Peter, H. J. Ohlbach, and P. Weber, private communication.
[23] J. B. Flanz, R. S. Hicks, R. A. Lindgren, G. A. Peterson, J. Dubach, and W. C. Haxton, Phys. Lett. **43**, 1922 (1979).
[24] E. M. Lyman, A. O. Hanson, and H. B. Scott, Phys. Rev. **84**, 626 (1951).
[25] K. Merle, Ph.D. thesis, University of Mainz (1976).
[26] W. Reuter, Ph.D. thesis, University of Mainz (1981).
[27] L. S. Cardman, S. P. Fivozinsky, J. W. Lightbody, Jr.,

X. K. Maruyama, E. A. J. M. Offermann, S. Penner, W. P. Trower, and S. E. Williamson (unpublished).
[28] T. de Forest, Jr. and J.D. Walecka, Adv. Phys. **15**, 1 (1966).
[29] B. Dreher, J. Friedrich, K. Merle, H. Rothhaas, and G. Lührs, Nucl. Phys. **A235**, 219 (1974).
[30] G. G. Simon, Ch. Schmitt, F. Borkowski, and V. H. Walter, Nucl. Phys. **A333**, 3 (1980).
[31] J. Borysowicz and J. H. Hetherington, Phys. Rev. C **7**, 2293 (1973).
[32] L. S. Cardman, J. W. Lightbody, Jr., S. Penner, S. P. Fivozinsky, X. K. Maruyama, W. P. Trower, and S. E. Williamson, Phys. Lett. **91B**, 203 (1980); **97B**, 473(E) (1980).
[33] J. A. Jansen, R. Th. Peerdeman, and C. de Vries, Nucl. Phys. **A188**, 337 (1972).
[34] P. R. Bevington, *Data Reduction and Error Analysis for the Physical Sciences* (McGraw-Hill, New York, 1969), Chap. 10.
[35] N. Kalantar-Nayestanaki, C. W. de Jager, E. A. J. M. Offermann, H. de Vries, L. S. Cardman, H. J. Emrich, F. W. Hersman, H. Miska, and D. Rychel, Phys. Rev. Lett. **63**, 2032 (1989).
[36] J. L. Friar and J. W. Negele, Nucl. Phys. **A240**, 301 (1975).
[37] W.-F. Lin, Phys. Lett. **39B**, 447 (1972).
[38] R. L. Mercer and D. G. Ravenhall, Phys. Rev. C **10**, 2002 (1974).
[39] H. G. Andresen and P. Weber, University of Mainz Annual Report, 1984–1985.
[40] J. L. Friar, Ann. Phys. (N.Y.) **98**, 490 (1976).
[41] J. L. Friar, Nucl. Phys. **A257**, 403 (1976).
[42] J. L. Friar, in *Proceedings of the International School on Electron and Pion Interactions with Nuclei at Intermediate Energies,* Arricia, 1979, edited by W. Bertozzi, S. Costa, and C. Schaerf (Harwood, New York, 1980), p. 143.
[43] L. A. Schaller, L. Schellenberg, T. Q. Phan, G. Piller, A. Ruetschi, and H. Scheuwly, Nucl. Phys. **A379**, 523 (1982).
[44] I. Sick, Phys. Lett. **116B**, 212 (1982).
[45] L. S. Cardman, J. Friedrich, C. W. de Jager, H. Miska, E. A. J. M. Offermann, and H. de Vries, Electron-Scattering Proposal 85-E18, NIKHEF-K (1985).
[46] V. Breton, P. Bricault, L.S. Cardman, B. Frois, D. Goutte, D.B. Isabelle, A.W. Linzey, G. Masson, L. Maximon, E.A.J.M. Offermann, X.H. Phan, S.K. Platchkov, I. Sick, and S.E. Williamson, Phys. Rev. Lett. **66**, 572 (1991).